# Combining phase field modeling and deep learning for accurate modeling of grain structure in solidification

Antoine Herbeaux, Hussein Aboleinein, Aurélien Villani, Claire Maurice, Jean-Michel Bergheau, Helmut Klöcker

Antoine Herbeaux, Hussein Aboleinein, Aurélien Villani, Claire Maurice, Jean-Michel Bergheau, et al.. Combining phase field modeling and deep learning for accurate modeling of grain structure in solidification. Additive Manufacturing, 2024, 81, pp.103994. 10.1016/j.addma.2024.103994 . emse-04488126

HAL Id: emse-04488126
https://hal-emse.ccsd.cnrs.fr/emse-04488126v1

Submitted on 4 Mar 2024

Additive Manufacturing 81 (2024) 103994

Contents lists available at ScienceDirect

Additive Manufacturing

journal homepage: www.elsevier.com/locate/addma

# Combining phase field modeling and deep learning for accurate modeling of grain structure in solidification

Antoine Herbeaux [a,*], Hussein Aboleinein [a], Aurélien Villani [a], Claire Maurice [a], Jean-Michel Bergheau [b], Helmut Klöcker [a]

[a] Mines Saint-Etienne, Univ Lyon, CNRS, UMR 5307 LGF, Centre SMS, F - 42023, Saint-Etienne, France
[b] Univ Lyon, École Centrale de Lyon, CNRS, ENTPE, LTDS, UMR5513, ENISE, 42023, Saint Etienne, France

ARTICLE INFO

*Keywords:*
316LSi
Cold Metal Transfer (CMT)
Microstructure
Optical and SEM observations
Artificial intelligence-based image segmentation & phase field approach

ABSTRACT

Additive manufacturing by wire deposition is a complex process as it generates overlapping and transient thermal fields, resulting in multiple cycles of solidification and remelting. Consequently, simulating the microstructure becomes challenging, making it difficult to optimize the process and predict the mechanical properties of an additive-manufactured part. In this work, a framework is developed, including several sequentially applied methods to obtain increasingly accurate information about the microstructure resulting from a wire deposition process. This framework is based on understanding experimental data and utilizing them as inputs to simplify the problem or accelerate numerical simulations. The experimental inputs consist of light optical images, SEM, and EBSD images. The methods developed here are initially geometric-based and then progress to shape recognition, unsupervised learning, and phase field modeling.

## 1. Introduction

Additive Manufacturing (AM) is a modern technology that builds components layer by layer from a 3D CAD model. This process is fully automated and enables the production of complex components difficult to manufacture with traditional subtractive methods. An overview of the most common AM techniques available is given in [1]. AM systems may be categorized in terms of the feed stock material or the energy source. Wire feed systems use different energy sources (electron beam, laser, arc) [2]. Garcia-Colomo et al. [3] published a comparison framework to select specific AM techniques in aerospace applications. Wire deposition is favored if high deposition rates and large build volumes are the main criteria.

In wire additive manufacture, single beads of material are deposited side by side and in successive layers to generate the desired 3-dimensional structure [1,2]. In wire arc additive manufacturing (WAAM), liquid droplets transfer heat to the melt pool from the wire electrode. Wire-feed additive manufacturing can use laser, arc welding, or electron beam as energy sources for metal deposition. Among these, arc welding-based AM is preferred due to its higher deposition rate, energy efficiency, safe operation, and lower cost. Arc welding processes, such as GMAW or GTAW, have high energy efficiency and are promising for manufacturing aerospace components with medium to large sizes. The metal transfer mode is a critical factor in determining the component properties during WAAM [4]. Research shows that the CMT pulse advanced process can control the porosity rate by adjusting heat input. Several review papers dedicated to wire arc additive manufacturing have been published over the last years [4–6]. Li et al. [6] highlight the close relation between process parameters and final microstructure. Zeng et al. [7] analyzed thoroughly the relation between process parameters and microstructure for NiTi deposited by wire arc Tungsten Inert Gas (TIG) technology. Several other microstructural analyses may be found. In the following we limit the literature on 316 L stainless steel.

Long et al. [8] deposited 316 L stainless steel using a Cold Metal Transfer (CMT) system with two different linear energy inputs (LEIs). The microstructure, mechanical properties, and fracture mechanisms of the steel were examined using various techniques. The steel was found to consist of α-ferrite and austenite dendrites, with primary dendrite spacing decreasing with lower LEI or higher cooling rates. Wen et al. confirmed the influence of the LEI on the primary dendrite spacing [9]. They showed that the δ-ferrite contents remain similar under both high and low LEI. Wang et al. [10] deposited 316 L stainless steel with CMT technique in two different arc modes (SpeedArc and SpeedPulse). They concluded that SpeedArc leads to higher tensile strengths than

---

* Correspondence to: Mines Saint-Etienne, 158 cours Fauriel, 42023, Saint-Etienne CEDEX 2, France.
*E-mail address:* antoine.herbeaux@emse.fr (A. Herbeaux).

https://doi.org/10.1016/j.addma.2024.103994
Received 20 July 2023; Received in revised form 13 January 2024; Accepted 18 January 2024

**Table 1**
Nominal chemical composition of 316LSi stainless steel wire.

| Element | C | Cr | Ni | Mo | Mn | Si | P | S | N | Cu | Fe |
|---|---|---|---|---|---|---|---|---|---|---|---|
| wt% | 0.01 | 18.5 | 12.2 | 2.5 | 1.8 | 0.81 | 0.02 | 0.01 | 0.05 | 0.23 | Bal |

SpeedPluse due to a finer solidification microstructure. Cunningham et al. [11] analyzed the influence of inter-layer cooling time on the microstructure of CMT deposited 316 L steel. Palmeira et al. [12,13] characterized the microstructure of 316 L deposited by CMT. They determined the separation lines between successive layers and a mean bead shape with indication of the growth directions. All the preceding publications clearly indicate a strong relation between the process parameters (Linear Heat Input, interlayer cooling time), the bead shape, the microstructure and the mechanical properties. These are valuable indications for microstructural models.

The microstructure of a material is determined by the solidification velocity and thermal gradient at the solidification front, which are controlled by various process parameters. Additive manufacturing creates complex patterns due to multiple remelting, which can only be accurately simulated using appropriate tools [6–12]. Different models, such as phase-field, cellular automaton, and Monte Carlo, are used to describe microstructure evolution during solidification [14,15].

The most popular models for solidification are cellular automaton and phase field models [15]. CA models combined with finite element approaches allow to model large-scale problems involved in casting [16–18]. Recently these models were applied to selective laser beam melting [19]. Liu et al. modeled microstructure evolution during additive manufacturing of Ti6Al4V by coupling a 1D phase field approach with a CA model [20]. This approach combines faster calculations of the CA models with kinetics issued from a 1D phase-field model and requires high symmetry of the fusion bed. The CMT process does not lead to these highly symmetric fusion beds [8–12]. Zinovieva et al. [21] published a 3D CA model of microstructure obtained by selective laser melting.

Phase Field (PF) models use a continuous field variable (order parameter) to describe a diffuse interface between two phases instead of a sharp interface [22,23]. Considering the order parameter as an independent state variable, allows for the consideration of non-equilibrium states. In 1993, year Kobayashi used a PF model to solve Stefan's problem of solidification in an undercooled melt [24].

Additive manufacturing creates complex microstructures [6–12], which depend on the process parameters controlling the bead shape [25–27]. While PF- and CA-models are particularly well-suited for simulations of grain nucleation and growth, they are limited to small scales compared to the typical bead sizes. Our framework (Section 3) includes a phase field (PF) model to describe crystal orientation, therefore, a faster approach for detecting microstructural discontinuities (the interfaces) prior to using PF models is adopted.

Additive manufacturing holds great potential for producing workpieces with controlled microstructures. Wire arc additive manufacturing creates *mm-sized beads with micron-sized microstructural defects* at the bead boundaries, necessitating a model that covers a range of length scales from micrometers (for the accurate description of solidification microstructures) to several mm for the bead interfaces.

Since Kobayashi's pioneering work in 1993 [24,28], Phase Field (PF) models have proven to be highly efficient for simulating microstructure genesis at the micron scale. However, these models demand significant computational resources and are not yet suitable for modeling entire beads, as required for a bead with a cross-sectional area exceeding $4 \times 4 mm^2$, as highlighted in reference [15]. To address this challenge and model the microstructure across the entire bead cross-section, which spans from the micron to the millimeter scale, a novel model framework is proposed in Section 3. This framework comprises a series of successive methods, each building upon the predictions of the previous one. The initial methods focus on characterizing the deposit at the millimeter scale and require minimal experimental input. The final two methods employ a Phase Field approach to characterize the microstructure of the bead.

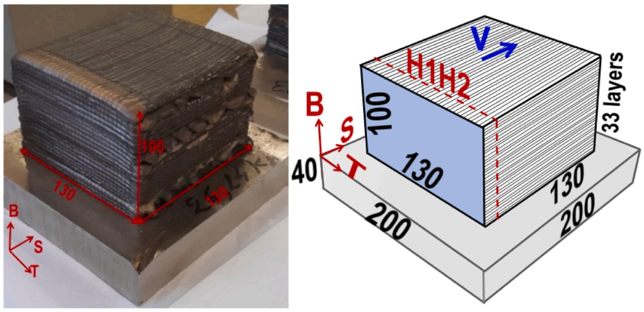

(a) (b)

**Fig. 1.** 316LSi stainless steel deposited by CMT (a) Sample, (b) schematic representation with annotations.

**Table 2**
CMT process parameters.

| Voltage (V) | Current (A) | (L/ min) | Wire feed (mm/s) | Travel speed (mm/s) | LEI (J/ mm) |
|---|---|---|---|---|---|
| 13.5 | 228 | 20 | 8 | 10 | 308 |

In Section 2, we present microstructural observations of 316 L stainless steel deposited by CMT. Section 3 details the development of a multiscale model of CMT based on minimal experimental input, utilizing various methods ranging from straightforward geometrical considerations to phase field modeling, and applying them to specific areas of the beads. The model's predictions are discussed in Section 4.

## 2. Experimental

### 2.1. Wire arc deposition and sample

Wire arc additive manufacturing was used to deposit 1.2 mm diameter 316LSi stainless steel wire onto a 304 stainless base plate measuring 200 × 200 mm with a thickness of 40 mm. The wire was supplied by Lincoln company and its chemical composition is given in Table 1. The resulting rectangular parallelepiped measured 130 mm × 130 mm x 100 mm (Fig. 1). A Fronius CMT torch mounted on a robot arm was used to deposit all the beads in the same direction (S) at a deposition angle of 0°. ARCAL™ Chrome (Ar - 2%C02) was used as shielding gas. The process parameters are indicated in Table 2, with a deposition rate of 4.23 kg/h and a step size of 4 mm. The deposition of each layer was carried out at room temperature, resulting in very long dwell times. The 316LSi density is 7960 $kg/m^3$. The total volume of the block is about 1755 $cm^3$, and its final weight, excluding the substrate, is about 14 kg.

### 2.2. Sample preparation

In the plane H1H2 perpendicular to the scanning direction (Fig. 1b), a sample was cut for microstructural observations. The dimensions of the sample H1-H2 are 89 mm × 57 mm x 10 mm. The sample was prepared for macroscopic observation using automatic polishing. The polishing process was followed by chemical etching by hydrofluoric acid

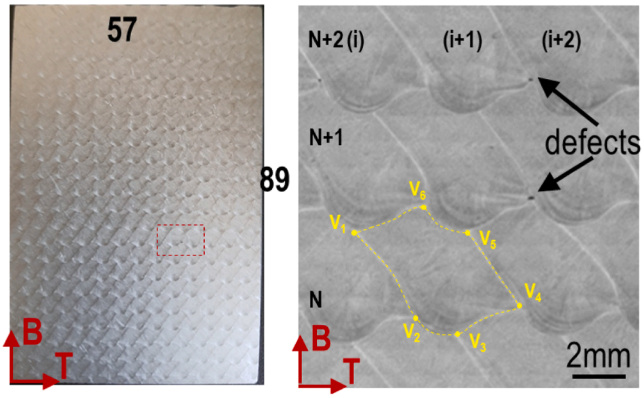

(a) (b)

**Fig. 2.** Section orthogonal to the scanning direction, light optical microscopic observation. (a) View of the entire section, (b) zoom on in the red rectangle in (a) showing the bead shape, the interfaces and defects at the junction of three beads. N, N + 1, N + 2 designate layers of material deposited successively; (i), (i + 1), (i + 2) correspond to beads in the same layer. The yellow dashed line shows the delimitation of a single bead.

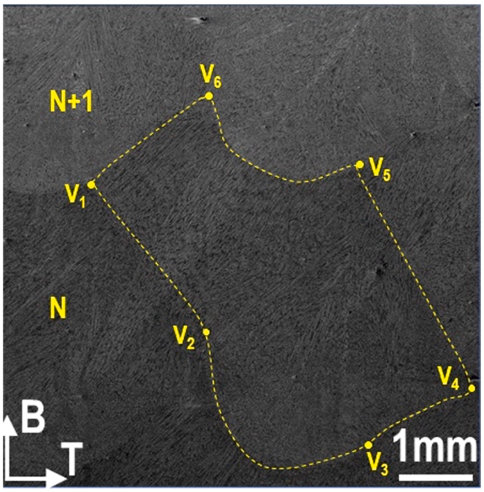

**Fig. 3.** SEM observation in a section perpendicular to the scanning direction. The light gray features correspond to δ ferrite and the dark gray matrix corresponds to austenite. N and N + 1 designate successive layers of material deposited. The yellow dashed line shows the border of a bead. $V_i$ are vertices defining the bead. $V_1$ to $V_4$ are formed during deposition of layer N. $V_5$ and $V_6$ are formed during deposition of layer N + 1.

with (40 ml HNO3, 10 ml HF and 10 ml H2O2). Etching lasted for 5 min 30 s in the acid at 60 °C. Samples for EBSD observations were extracted from the center of the block and prepared with standard surface finish for EBSD observations.

### 2.3. *Microstructural observations*

Fig. 2 depicts the entire sample H1H2 and zooms in on specific beads, with the borders being easily distinguishable. The vertices defining a particular bead are indicated in Fig. 2b, with the numbers N, N + 1, N + 2 indicating successive layers, and the numbers (i), (i + 1), (i + 2) indicating successive beads in the same layer. A typical bead shape can be defined by six vertices ($V_1$,…,$V_6$), as illustrated in the zoomed-in view in Fig. 2b. During the deposition of layer N, vertices ($V_1$,…,$V_4$) are formed, while vertices ($V_5$,$V_6$) are formed by the partial remelting of layer N during the deposition of layer N + 1. This partial remelting controls the material continuity, and its absence leads to the typical defects displayed in Fig. 2b. In Section 4, we will establish that the presence of defects also affects the bead shape and consequently the local microstructure.

Defects can arise due to the presence of gas bubbles and insufficient local remelting. In this paper, we do not delve into the analysis of process optimization. The responsibility for addressing and eliminating defects by selecting the appropriate process parameters is entrusted to industrial companies. Our primary focus is on describing the microstructure. However, given that defects can impact the shape of the lower contour, we do consider the influence of such defects on the contour's shape.

The light optical observations provide valuable information on the bead shape, which serves as the initial input for the model proposed in Section 3. Additionally, SEM observations were conducted to gather more data. Fig. 3 displays a composite image of a typical bead, revealing a mixture of δ ferrite (light gray) and austenite (dark gray). For pedagogical purposes, the bead border and corresponding vertices are highlighted in yellow. The δ ferrite density varies within the bead, and the orientation of the δ ferrite dendrites relative to the bead border is considered as an input for the model. Furthermore, zones with epitaxial grain growth between successive beads can be identified.

The microstructural analysis was completed with texture analysis through EBSD measurements. Inverse pole figures (IPF) are color-coded images where the colors are based on the standard stereographic triangle (for cubic symmetry), which is shown on the right. Each map represents the crystallographic direction aligned with one of the sample directions, scan, transverse or build. In Fig. 4(a,b), Inverse pole figures of γ-austenite in the S and T direction are shown. The $< 100 >$ directions correspond to the growth of the dendrites. The scanning direction is close to $< 001 >$. Two growth directions ($<100 >$ and $<010 >$) lie in the (B, T)-plane, but they form an angle of $\pm \pi/4$ with the B and T directions. The EBSD maps provide the final input for the model presented below. Fig. 4(c, d, e) represent inverse pole figures of γ-austenite in the B and S direction. Fig. 4(c–e) reveal the presence of large voids (indicated by white/red arrows), located at the layer base and elongated along the scan direction. These voids correspond to the defects used in the contour classification method. Fig. 4(c, d, e) reveal periodicity along the S axis. Based on this periodicity, a 2D grain growth model is used. Fig. 4f,g depict pole figures of ferrite and austenite. These figures show that the crystal orientations of ferrite and austenite are close.

## 3. Multiscale model of wire arc deposition

### 3.1. *Model layout*

The microstructural features discussed above span several orders of magnitude. Some defects at the mm-sized bead interface extend over several hundred μm, affecting the bead shape and the solidification microstructure. SEM images revealed μ-sized δ-dendrites with a non-homogeneous distribution inside the bead. EBSD observations showed an overall crystal orientation with growth directions perpendicular to the bead border, with complex grain shapes and orientations at the center of the remelted zone.

To model the microstructure, a combination of different methods suited for specific length scales is necessary. The proposed model uses five methods applied successively (Fig. 5), starting with light optical microscopy to observe large surfaces at low cost. Method M0 extracts different beads, while method M1 predicts crystal orientations based on mean bead shapes. Method M2 constructs a complete bead by translation of a given pattern, leading to a periodic mesh of the 2D space. Adjacent zones in different beads correspond to different deposition times.

Method M3 uses superpixel segmentation and a Convolutional Neural Network (CNN) model to analyze the SEM image shown in Fig. 3 and identify the continuity of microstructure at the intersection of three beads. Method M4 utilizes a PF approach to analyze a complete bead,

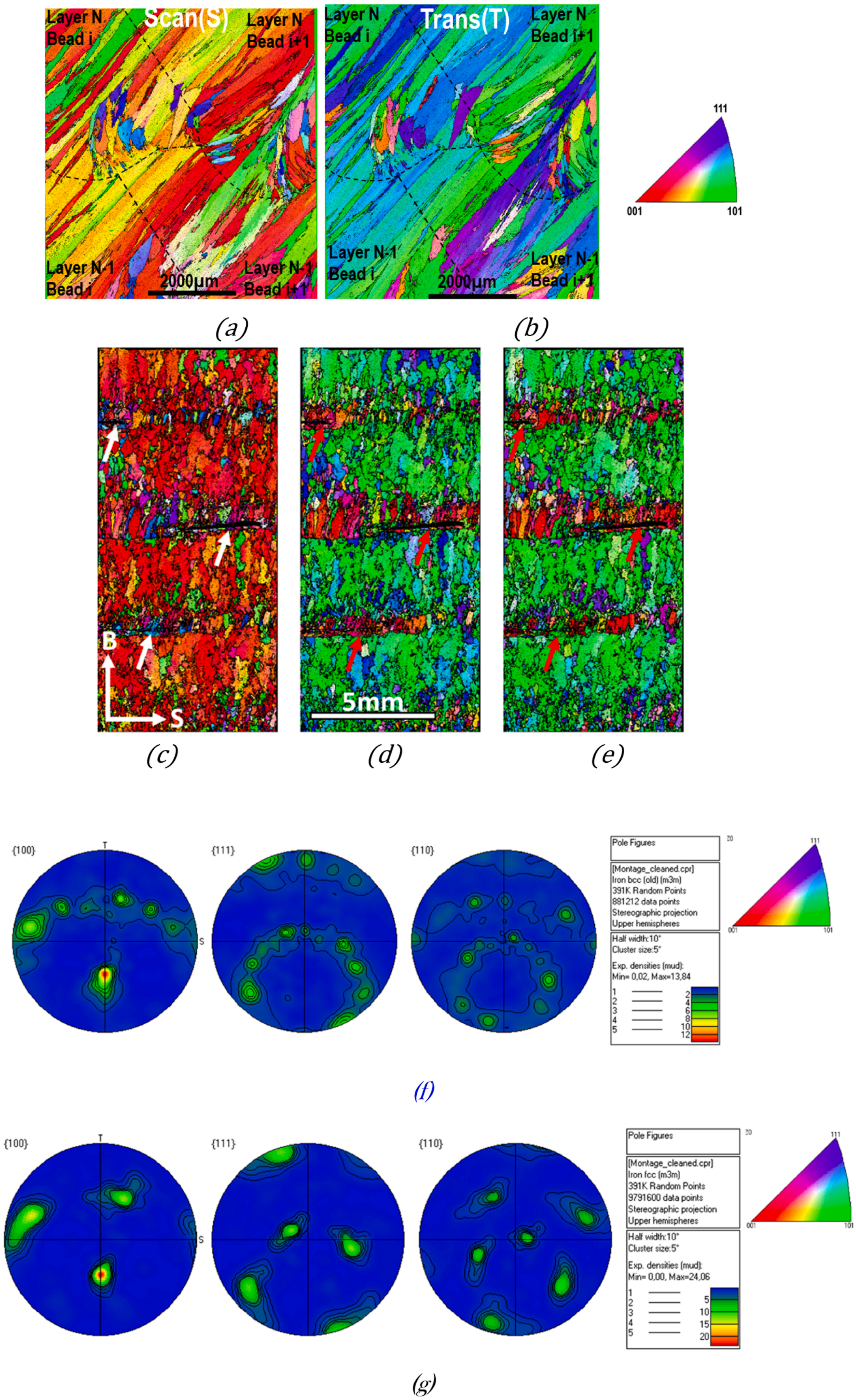

*(a)* *(b)*

*(c)* *(d)* *(e)*

*(f)*

*(g)*

**Fig. 4.** EBSD characterization. IPF maps of γ -austenite (a) scanning direction, (b) transverse direction. The dashed lines indicate bead boundaries, (c-e) pole figures in the BS plane showing periodicity at the scale of a bead. Poles figures of ferrite (f) and austenite (g).

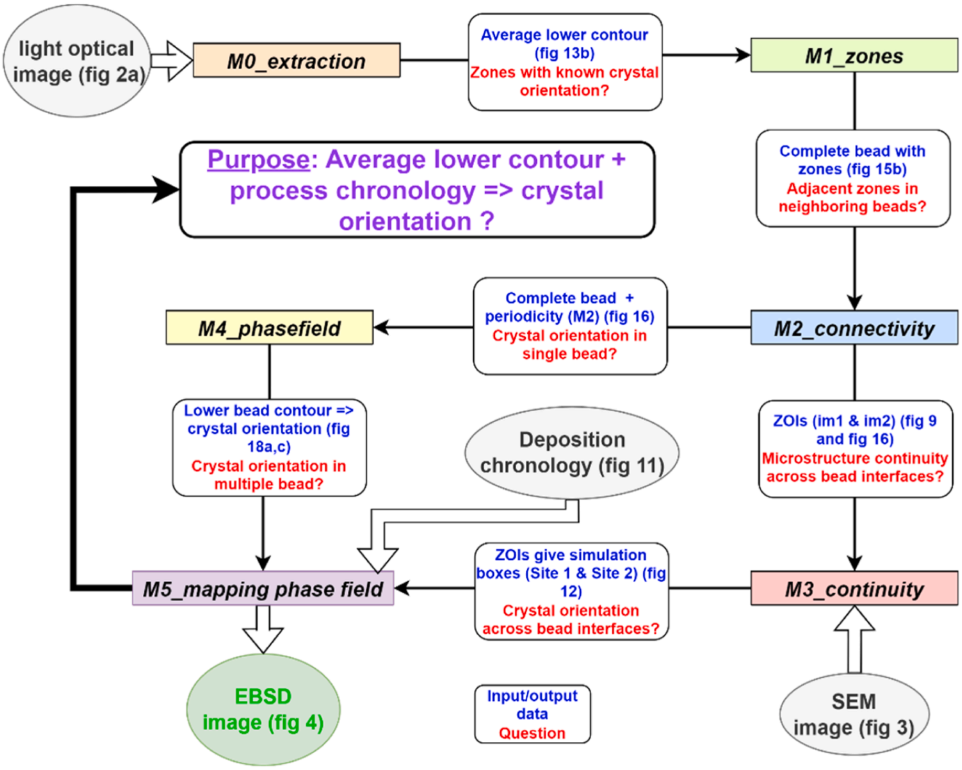

**Fig. 5.** Model layout. M0 to M5 indicate successive methods. The data transfers from one method to the next are indicated by dark arrows. Bold light grey arrows indicate experimental input.

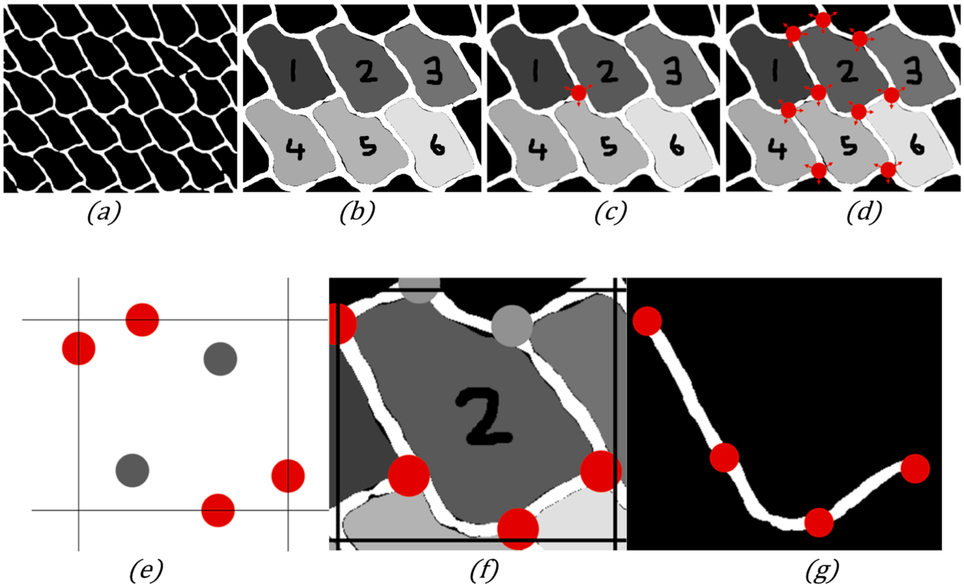

**Fig. 6.** Detailed information for the set-up of method M0, the extraction of the lower bead contour.

while method M5 considers multiple beads that have been deposited in succession and models them using a PF approach, thus considering the remelting that occurs at the interfaces between the beads.

Method M0 (contour extractions) relies on optical observations, which are cost-effective. In contrast, Method M4 (Phase field simulations) predicts local grain structure and is computationally intensive. However, leveraging input from Method M0 significantly accelerates computations in Method M4. Both Methods M0 and M4 can be used independently.

Method M3 (AI based segmentation) involves SEM observations, which are relatively more expensive, though their utility is limited. Lastly, Method M5's (Mapping by phase field simulations) predictions are compared to EBSD observations, which are costly. Nonetheless, all model predictions can be used without necessitating a comparison to EBSD observations.

### 3.2. *Method M0: determine the lower part of bead contours*

Fig. 6 depicts the principle of Method M0. In Step 1, an image with identifiable objects is taken as input and cropped to contain the desired

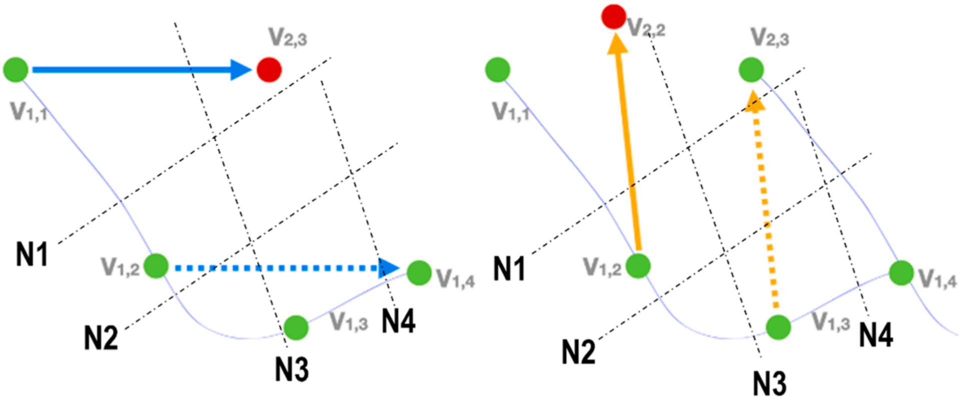

**Fig. 7.** Method M1: At the beginning of the method vertices $V_{1,i\ (i=1,..,4)}$ are known. Vertices $V_{2,2}$ and $V_{2,3}$ are determined by M1 based on the periodicity at the bead scale.

number of beads with defects on the right, defects on the left, and beads without defects, using the light optical observations from Fig. 2. Fig. 6a displays a selection of 30 beads.

In Step 2, the image is converted to grayscale, and a thresholding algorithm is employed to delineate the contours and beads, as depicted in Fig. 6b. An algorithm for nearest neighbor recognition is used to automatically number the beads from left to right and top to bottom, as illustrated for six beads in Fig. 6b. It's crucial for the white contours to be closed since the algorithm relies on the continuity of grayscale values; a completely black area is numbered, then incremented for the next area. A secondary grid is used to store the numbers of each pixel associated with its bead. Using the same nearest neighbor recognition algorithm, but with slight modifications, the triple points are determined, i.e., those with the smallest average distance between three numbered areas (Fig. 6c).

In Step 3, an algorithm browses through the grid of numbered beads and associates each one with the coordinates of the six nearest triple points to the "bead" zone, as highlighted for beads 2 and 5 in Fig. 6d. At this stage, a bead is characterized by an area of continuously numbered pixels and six triple points with coordinates (x, y).

In Step 4, the bounding box of each bead is determined (Fig. 6e). This box is defined by the lines passing through the points having the largest absolute values of x and y. It may be necessary to widen the box by a few pixels so as not to cut off a possible very curved contour, especially in the melting bath. These operations are depicted in Fig. 6e,f. Each bead is successively cut out of the original image.

In Step 5, the lower part of the contour of each bead is extracted (Fig. 6g). First, the coordinates of the continuous contour (in white in the original image) passing through the four triple points with the smallest y-coordinate values are determined. The points of the lower contour are then saved in an array with multiple entries for each x coordinate. For each x-coordinate, only the points equidistant between its minimum and maximum y-coordinate are considered: leading to a contour with zero thickness. This new lower contour is fitted with a cubic spline (Univariate Spline function from SciPy). The process is repeated for all beads to obtain the representative spline of each lower contour. For each family, the average of all splines of each lower contour is taken to obtain the specific mean lower contour for each family.

Method M0 is completed automatically except for the detection of defects. This is the sole part left to appreciation by the human eye. The CPU time needed is negligible, so that the method can easily be applied to several thousands of objects, even on a classic workstation. The method M0 delivers the equations of 3 typical beads, i.e., with a defect to the left, with no defect and with a defect to the right. Vertices $V_1$ and $V_4$ correspond to the end points of the lower bead. The intermediate vertices $V_2$ and $V_3$ correspond to points where changes in curvature are observed. Method M0 has given an analytic description of the lower contour of the 3 kinds of beads (defect to the left, the right or no defect).

### 3.3. Method M1: determine the upper part of bead contours and predict local crystal orientation

Method M1 consists also of several consecutive steps. Several combinations of beads with and without defects can pave the entire 2D space. Currently, the aim is to reconstruct the three entire beads from the knowledge of the mean curve representing their lower part. Thus, mapping the 2D space with a single elementary motive (with or without a defect) is considered. Mapping the space with a combination of the red, blue, green motives would follow the same steps. At the beginning of method M1, the vertices $V_1$,i (i = 1,2,3,4) representing the lower boundary of a bead are known.

In step 1, vertices $V_{2,2}$ and $V_{2,3}$ are determined (Fig. 7). First vertex $V_{2,3}$ is determined by $\overrightarrow{V_{1,1}V_{2,3}} = \overrightarrow{V_{1,2}V_{1,4}}$. Once, $V_{2,3}$ is known, the coordinates of $V_{2,2}$ are given by $\overrightarrow{V_{1,2}V_{2,2}} = \overrightarrow{V_{1,3}V_{2,3}}$.

In step 2, the bead is divided in different regions defined by the curvature of the lower contour. Lines N1 to N4, normal to the lower contour, are drawn and divide the bead surface into typical zones. First the zones defined by one single normal to the lower contour are determined. These will be labeled by single integers 1a to 2c as depicted in Fig. 15. Interior zones corresponding to the crossing of different lines normal to the lower contour are labeled with the two or three corresponding single digit integers.

Until here, only geometrical considerations prevailed. At this stage, the following assumption is made. Deposition of layer N causes remelting of the material in layer (N-1). This remelting stopped at the lower bead border. Hence, nucleation of the new bead (in layer N) starts at the lower bead border. Locally the temperature gradient is perpendicular to the lower bead border. The growth direction ($<100>$) is parallel to the temperature gradient [29]. Hence, all zones defined by a single normal are considered to have a known $< 100 >$ direction. This assumption will be checked by method M4 and EBSD observations.

### 3.4. Method M2: bead construction and further definition of crystallographic zones

At this stage, the bead shape is defined and the crystal orientation in zones adjacent to the lower contour is known. Considering the periodicity of the deposit, will lead to further insight. In step 1, method M2 maps the entire plane with the elementary bead and the corresponding zones determined by method M1. In step 2, zones in adjacent beads are considered. Periodicity implies that zones adjacent to a *single* numbered one in the neighbor bead also exhibit a known growth direction $< 100 >$.

The distribution of defects is not "homogeneous" across the deposit.

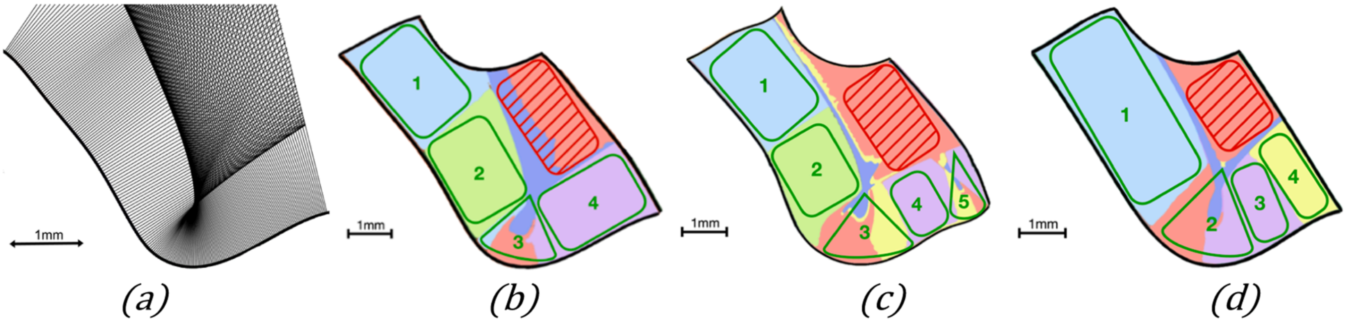

**Fig. 8.** Test results of CNN. The CNN was applied with the parameters given in Tables 3 and 4 and as input, the images with the normals to the lower contour in (Fig. 14 a, b, c). Figure (a) shows the input used for the contour without defect. Figures (b-d) show results corresponding respectively to contours with defect to the left, no defect and a defect to the right. Different colors correspond to different zones detected by the CNN algorithm.

This distribution is influenced by minor variations in the process parameters. Fig. 14 illustrates the construction with four contours for each type of bead: those without defects and those with defects. While it would be feasible to construct a complete bead solely based on contours with defects (on the left and right), mapping the 2D space with such a bead is not realistic. In the current work, the 2D space has been mapped using beads without defects.

### 3.5. *Method M3: deep learning algorithm for continuity analysis of the microstructure at bead interfaces*

Deep learning is commonly used for microstructure classification. In 2008, de Albuquerque et al. [30,31] proposed using artificial neural networks for simple nodular microstructure classification from cast iron images. However, supervised learning algorithms require many labeled datasets. In WAAM depositions, microstructural discontinuities are suspected at the boundaries of mm-sized beads, and their characterization requires several hundred SEM images for a single bead, making it inefficient to train an algorithm with images of several beads. To address this issue, Kim et al. [32] developed an unsupervised segmentation algorithm for light optical images of low carbon steel in 2020, based on a superpixel segmentation technique [33–37]. The algorithm utilizes important user-defined parameters, including the number of superpixels and the compactness factor m, and a CNN computation to derive a feature for each region. The network is trained to select the most frequent feature in each region, and several commonly appearing features are automatically selected. A loss function is employed to measure the disparity between the CNN output image and the refined image during the algorithm's training [32].

At the end of method M2, all possible predictions based on the bead shape and perfect periodicity at the bead scale have been made. All zones where the $< 100 >$ direction could be determined by these simple arguments have been identified. At this stage, microstructure continuity (in the sense of identical crystal directions) between adjacent beads has been answered everywhere except at the zones corresponding to the junction of 3 beads. To analyze the continuity of the microstructure between two adjacent beads, the deep learning algorithm published by Kim et al. [32] was used. In the current analysis, SEM observations are needed to characterize microstructural discontinuities. The Light optical micrographs in [32] exhibit large differences in shape and contrast (color). The SEM observations in Fig. 3 exhibit essentially differences in the density of δ-dendrites in an austenite matrix. To ascertain the usefulness of the algorithm for this kind of observations, the method was tested on synthetic microstructures. As input the contours similar to Fig. 14 a, b, c (predicted by method M1) were used. However, a much higher density of the lines normal to the lower contour, were used as input to the algorithm. This input (based on M1) was intended to reproduce "crystal" growth directions. Fig. 8a shows an example input corresponding to the bead without defects. We intentionally used an image difficult to analyze to test the CNN model. The compactness m and the number of superpixels used are given in Table 3. The parameters used in the CNN model are given in Table 4. With these parameters, application of the unsupervised learning algorithm to the input generated by method M1 leads to the output depicted in Fig. 8.

**Table 3**
Parameters used for superpixel definition.

| Superpixel model parameters | Number of superpixels | Compactness value |
|---|---|---|
| values | 1000 | 10 |

**Table 4**
Parameters used in the CNN model.

| parameter | Number of channels | Maximum of iterations | Minimum number of labels | Learning rate for training | Number of convolutional layers |
|---|---|---|---|---|---|
| values | 100 | 2000 | 10 | 0.1 | 8 |

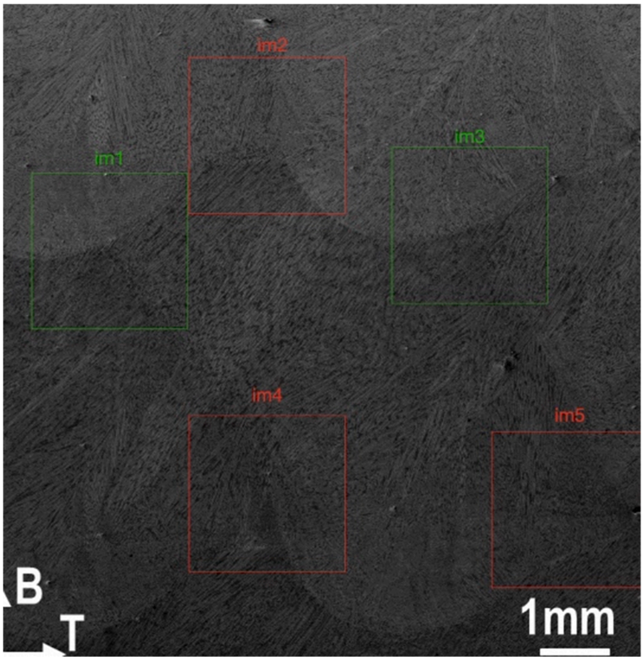

**Fig. 9.** SEM image used as input to the CNN algorithm with the ZOIs indicated in green and red.

Application of the CNN algorithm to Fig. 8a leads to the different zones represented in Fig. 8c (bead without) defect. Similar analyses were made for the bead shapes with a defect. The aim is to test the CNN algorithm before using it on the SEM image. The different colors in Fig. 8 correspond to different patterns detected by the CNN algorithm. During the zone recognition test, the neural network successfully identified all the lower zones but struggled to identify the upper zones. It mistakenly categorized the radial zone, corresponding to the remelted material, as two separate zones because it perceived a 50% growth towards the right and 50% towards the left. This is an artifact due to the test image (Fig. 8a). On the SEM image (Fig. 9), we consider the remelted zone as a single entity. The test case represented by Fig. 8a is more difficult to analyze then the real SEM image. Hence, despite this limitation, given the accurate prediction of zones by drawing normals to the lower contour, the validated model instills confidence in its applicability to the scanning electron microscope (SEM) image. The synthetic image was kept intentionally more difficult to analyze than the real SEM image.

The neural network has been applied to the SEM observation. Regions of interest of 1500 × 1500 pixels centered on triple points were defined. There are 5 triple stitches per bead. However, the regions of interest im1 and im3 are identical by translation (periodicity of the process). The same is true for regions im2, im4 and im5. So only two regions were chosen: im1 and im2.

### 3.6. *Method M4: phase field approach for crystal orientation inside the entire bead*

In this section we focus mainly the PF models dedicated to solidification. Widespread applications of PF models are given in many overviews [22,23]. PF models use a continuous field variable, generally called order parameter, to describe a diffuse interface between two phases instead of a sharp interface with a discontinuity in material properties. Seeing the order parameter as an independent state variable, allows for the consideration of non-equilibrium states. Cahn and Hilliard [38] used the alloy concentration itself as the order parameter for spinodal decomposition. In 1993, Wheeler et al. [39] analyzed solute trapping during solidification with a PF approach. The same year Kobayashi developed a diffuse interface scheme to solve Stefan's problem of solidification in an undercooled melt [24]. Kobayashi's model considers a diffusion equation for the temperature $\mathrm{T}(\vec{x},\mathrm{t})$ and an evolution equation for the scalar phase field $\phi(\vec{x},\mathrm{t})$, which distinguishes the solid ($\phi = 1$) and the liquid ($\phi = 0$) phases through a smooth transition.

$$\dot{T} = \nabla(D_T \nabla T) + \frac{L}{C_p}\dot{\phi} \tag{1}$$

$$\tau\dot{\phi} = \epsilon \quad \nabla^2\phi + \gamma\phi(1-\phi)\left[\phi - \frac{1}{2} + m(\phi)(T_m - T)\right] \tag{2}$$

Eq. (1) describes heat diffusion with an additional term for the latent heat L of a pure substance with melting temperature $\mathrm{T_m}$ and heat capacity $\mathrm{c_p}$. In Eq. (2), ε and γ are proportional to the interface energy and τ is a relaxation time. The presence of $\dot{\phi}$ in Eq. (1) and $(\mathrm{T_m} - \mathrm{T})$ in Eq. (2) leads to strong coupling of both equations. In 1998, Kobayashi et al. [28] introduced a vector valued order parameter to describe crystal misorientations. They considered the following energy functional:

$$E = \int_{\Omega} dV\left[\frac{\epsilon^2}{2}|\nabla\Phi|^2 + \frac{\mu(\Phi)}{2}\Phi^2|\nabla\theta|^2 + f_{dw}(\Phi, m)\right] \tag{3}$$

The order parameter, Φ, distinguishes between solid and liquid states, while θ represents local crystal orientation. The double-well potential, $\mathrm{f_{dw}}$, has minima in both the solid (Φ =1) and liquid (Φ =0) states. The parameter m differentiates between solid disordered and crystalline phases, while ε accounts for anisotropic surface energy. The energy functional's second term assumes that the energy changes due to the misorientation of adjacent grains only depend on $|\nabla\theta|^2$. As this model leads to instabilities at low interface energies, the authors presented a modified model ensuring stability in 2000. Boettinger et al. [40] used a similar approach, where the energy functional explicitly depended on solute concentration. They applied this new model to various metallurgical problems associated with solidification. The present paper utilizes the 2D PF approach based on Warren et al. [41], which has two field parameters: an orientation θ and a phase Φ. This model is governed by the following functional:

$$F = \int_{\Omega} dV\left[f(\phi, T) + \frac{\alpha^2\Gamma^2}{2}(|\nabla\phi|, \theta - \psi) + sg(\phi)|\nabla\theta| + \frac{\epsilon^2}{2}h(\phi)|\nabla\theta|^2\right] \tag{4}$$

The field parameter $\phi$ describes crystalline order (0 in a disorder phase and 1 in a perfect crystal). Hence, $\phi < 1$ may be observed in grain boundaries. The field θ measures the crystal orientation with respect to a fixed reference frame. For crystals with an N-fold symmetry $\theta \in [-\pi/\mathrm{N}, \pi/\mathrm{N})$. The grain boundary properties may be a function of its inclination. ψ describes the inclination of the liquid solid interface with respect to the x-axis. Γ allows considering anisotropic grain boundary energies (Eq. (3) in Warren et al. [23]). s and ϵ control the coupling between $\phi$ and ∇θ. $\mathrm{g}(\phi)$ and $\mathrm{h}(\phi)$ must be monotonic functions. The linear term |∇θ| avoids grain boundaries to spread out without limitation. The nonlinear term $(|\nabla\theta|^2)$ revealed essential to describe grain boundary motion. In a recent papers Xue et al. [42] consider the free energy as a loss function to minimize by unsupervised learning, leading to reduced computational time. In [43], Choi et al. apply this resolution method to powder laser melting.

Phase field approaches have been successfully applied to model solidification microstructures in the past. Steinbach's review paper [22] provides an overview of the use of PF models in material science, while Plapp's review [23] focuses on the application of PF models to solidification problems. Recent reviews by Gatsos et al. [14] and Körner et al. [15] have focused on the simulation of microstructure evolution for additive manufacturing of metals. PF frameworks enable the modeling of nucleation of new grains, but they require extremely fine meshes or cells, making them suitable for modeling small volumes. Therefore, these approaches are particularly suited for modeling the microstructure at bead/layer interfaces.

At the end of method M2, all possible predictions based on the bead shape and perfect periodicity at the bead scale have been made. Method M3 detects potential discontinuities in the microstructure. A phase field approach based on Warren et al. [23] is used to confirm the crystal orientation in an entire bead section. The same approach will be applied in the next section with a finer scale at the discontinuities detected by method M3.

The aim of present work is the prediction of local crystal orientations. One might think that solute trapping needs to be modeled for predicting local textures. However, solute trapping primarily influences the solid-solid transformation from ferrite to austenite. Inoue et al. [29] demonstrate that ferrite and austenite exhibit the same orientation, a finding confirmed by our EBSD observations (Fig. 4f,g). Furthermore, the distributions of ferritic and austenitic phases are nearly uniform in the bead. Therefore, considering solute trapping does not appear to be necessary for predicting crystal orientation.

Three strongly coupled equations are solved simultaneously. The first one describes heat diffusion in the bead section. The additional term $(\partial\phi/\partial t)$ corresponds to the latent heat of solidification.

$$\frac{\partial\Delta T}{\partial t} = D_T\nabla^2\Delta T + \frac{\partial\phi}{\partial t} \tag{5a}$$

$\Delta T$ stands for the non-dimensional undercooling.

$$\Delta T = \frac{T - T_m}{T_m - T_0} \tag{5b}$$

In expression (5b) T, $T_m$ and $T_0$ represent respectively the current, the melting and the room temperature. Similarly, $D_T$ and $\phi$ are given by:

**Table 5**
Definition of the characteristic parameters used in equations (6) and (7) and their corresponding non-dimensional expressions. Values taken from [41].

| | | | | | | |
|---|---|---|---|---|---|---|
| $\tau_\phi = \frac{6L\delta}{\mu T_m}$ | $\alpha^2 = 6\sigma_{l/s}$ | $a = \sqrt{L/2}$ | $\tau_\theta = 10\tau_\phi$ | $\epsilon = \frac{\alpha}{1.875}$ | $s = 1.25a\epsilon$ | $\kappa_1 = 0.9$ |
| $\widetilde{\tau_\phi} = \frac{\tau_\phi}{a^2 t_0}$ | $\widetilde{\alpha} = \frac{\alpha}{al_0}$ | $\nu = 1000$ | $\widetilde{\tau_\theta} = \frac{\tau_\theta}{a^2 t_0}$ | $\widetilde{\epsilon} = \frac{\epsilon}{al_0}$ | $\widetilde{s} = \frac{s}{al_0}$ | $\kappa_2 = 20$ |

$$D_T = \frac{\lambda}{\rho c_p}\frac{\partial \phi}{\partial t} = \frac{L}{c_p(T_m - T_0)}\frac{\partial \Phi}{\partial t} \tag{5c}$$

a, ρ and $c_p$ correspond to the thermal conductivity, density and heat capacity of the solid phase. L represents the latent heat per unit mass.

$$\Phi_{liquid}(\overrightarrow{x}) = 0\Phi_{solid}(\overrightarrow{x}) = 1 \tag{5d}$$

Equations (6) and (7) give the non-dimensional forms for the evolution of the phase value $\phi$ and the crystal orientation θ. All the physical dimensions of the parameters used in the phase field approach are given in the Appendix (Table 9).

$$\widetilde{\tau_\phi}\frac{\partial \phi}{\partial t} = \widetilde{\alpha}^2\nabla^2\phi + \phi(1-\phi)m(\Delta T, \phi) - 2\widetilde{s}\phi|\nabla\theta| - \widetilde{\epsilon}^2\phi|\nabla\theta|^2 \tag{6a}$$

$$m(\phi, \Delta T) = \phi - \frac{1}{2} - \frac{\kappa_1}{\pi}\arctan(\kappa_2 \Delta T) \tag{6b}$$

$$P(\widetilde{\epsilon}|\nabla\theta|)\widetilde{\tau_\theta}\frac{\partial \theta}{\partial t} = \nabla.[\phi^2\left(\frac{\widetilde{s}}{|\nabla\theta|} + \widetilde{\epsilon}^2\right)\nabla\theta] \tag{7a}$$

$$P(\widetilde{\epsilon}|\nabla\theta|) = 1 - e^{-\beta\widetilde{\epsilon}|\nabla\theta|}(1 + \frac{\widetilde{\nu}}{\widetilde{\epsilon}}) \tag{7b}$$

$$\beta = \frac{1-\psi^2}{1+\psi^2} \quad \psi = \tan(\frac{N}{2}(\theta + \arctan(\frac{\frac{\partial\phi}{\partial y}}{\frac{\partial\phi}{\partial x}}))) \tag{7c}$$

$\tau_\phi$ and $\tau_\theta$ are characteristic times for the phase equation and the crystal orientation. s and ϵ introduce first and second order coupling between the phase equation and the crystal orientation. Table 5 summarizes the expressions of the characteristic constants and the corresponding non-dimensional expressions. For the purpose of defining non-dimensional parameters, a characteristic length ($l_0$) and time ($t_0$) have been introduced as follows:

$$(\widetilde{x}, \widetilde{y}, \widetilde{z}) = (\frac{x}{l_0}, \frac{y}{l_0}, \frac{z}{l_0})\widetilde{t} = \frac{t}{t_0} \tag{8}$$

In table 5, L stands for the latent heat of fusion, $T_m$ for the melting temperature and δ for the liquid/solid interface thickness, whereas μ represents a kinetic linear coefficient. $\sigma_{l/s}$ is the liquid solid interface energy.

The following physical values are thus needed to define all the parameters in equations (5), (6), (7). The input parameters for the heat equation are ρ, $c_p$, $D_T$ and $T_m$. On the other hand α, L, δ, $\sigma_{l/s}$ and μ are material parameters used to calculate phase field parameters. The following parameters are chosen by the user of the model: the temperature $T_0$, the characteristic time $t_0$ and the characteristic length $l_0$. All the parameters mentioned are given in Table 6. Additional parameters specific to the numerical modeling are given in Table 7. The initial and boundary conditions might be found in (Table 8).

The deposition of a welding bead occurs only after waiting for the temperature of the workpiece to sufficiently drop. The initial temperature of the solid steel is therefore set to 400 K. To ensure the preservation of the liquid droplet volume, solidification is strictly confined to the yellow region in Fig. 10. In the same figure, the white area represents air and thus remains unaffected by the phase change. It becomes relevant solely in resolving the thermal equation for convective heat dissipation. The droplet's initial temperature is set at 2000 K, slightly above the molten steel's temperature. A homogeneous and random distribution of grains was considered in the substrate. This distribution leads to nucleation at the liquid solid interface. No nucleation in the liquid was considered. But the model allows simulating this nucleation. After applying the necessary conditions, the simulation is initiated, and the differential equations are solved using the finite volume solver FiPy [44].

The thermal simulation commences following the deposition of the droplet and the partial remelting of the previous layer. To account for potential heating from adjacent material in the S direction, we ensure that the droplet remains above the liquidus temperature for a duration of 60 ms. Initially, we assume a uniform thermal field within the droplet.

Given the challenging nature of predicting the geometry of the remelted zone [42,43], we determine the shape of the remelted zone based on experimental data (see Fig. 2). Fig. 10c-f illustrate the evolution of the thermal field after the deposition of the droplet. The observable thermal gradient is a result of heat exchange with the colder substrate.

EBSD maps, as shown in Fig. 4, confirm that $< 001 >$ corresponds to S. Our specific interest lies in the directions $< 100 >$ and $< 010 >$ within the (B, T) plane, which are influenced by the components of the thermal gradient within this plane. These crystallographic directions can be obtained through 2D simulations.

### 3.7. Method M5: phase field approach for the simulation of bead interfaces

The objective of this method is to reveal the continuity of dendritic growth at the boundaries of adjacent beads. Specifically, it examines the interface with the following bead and with the upper bead of the next layer. To achieve this, the same regions of interest as in M3 (im2 and im3), which are boxes centered on the two triple points of interest) are

**Table 7**
Additional model parameters used in the phase field approach.

| Model Parameters | Number of Elements | Element size | Time step |
|---|---|---|---|
| Values | 800 | 0.2 | $5\ 10^{-4}$ |

**Table 8**
Boundary conditions and initial values used in the PF approach.

| Temperature Zone 1 | Temperature Zone 2 | Temperature Zone 3 | Phase Zone 1 | Phase Zone 2 | Phase Zone 3 |
|---|---|---|---|---|---|
| 400 K | 293 K | 2000 K | Solid | Air | Liquid |

**Table 6**
Values of the parameters used in the phase field approach. $N_{fold}$= 4 symmetry was considered.

| Heat equation | | | | Phase and orientation | | | Control parameters | |
|---|---|---|---|---|---|---|---|---|
| $D_T$ $\left(m^2 s^{-1}\right)$ | $L$ $(Jm^{-3})$ | $T_m$ $(K)$ | $T_0$ $(K)$ | $\sigma_{l/s}$ $(Jm^{-2})$ | $\mu$ $(\frac{m}{K.s})$ | $\delta$ $(\mu m)$ | $t_0$ $(s)$ | $l_0$ $(m)$ |
| $12.10^6$ | $2.10^9$ | 1811 | 293 | 1.8 | 2.2 | 0.1 | $10^{-4}$ | $22.10^{-6}$ |

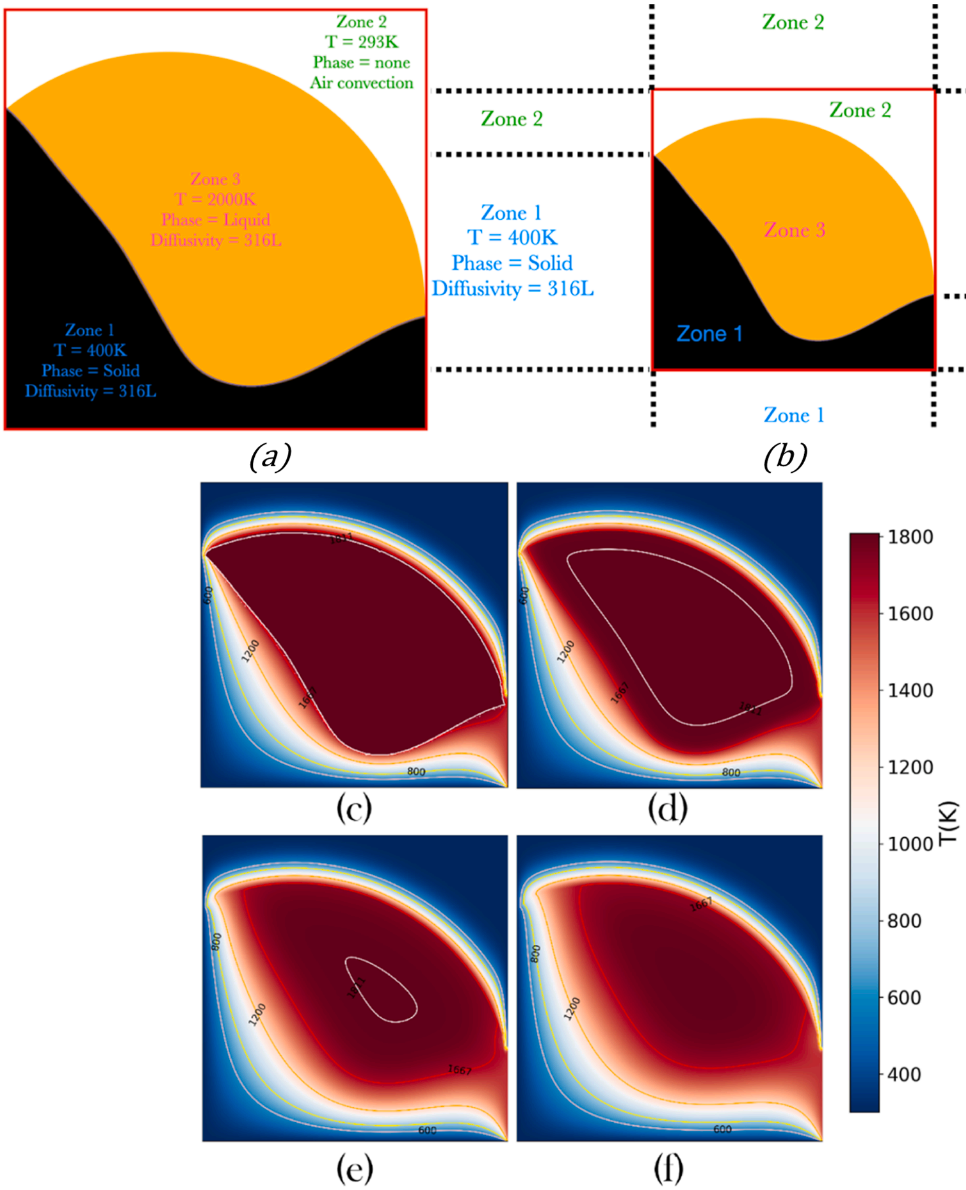

**Fig. 10.** Initial (a) and boundary conditions (b) as input for phase field simulation of bead solidification, (c) temperature field after respectively 60 ms (c), 66 ms (d), 72 ms (e), 78 ms (f).

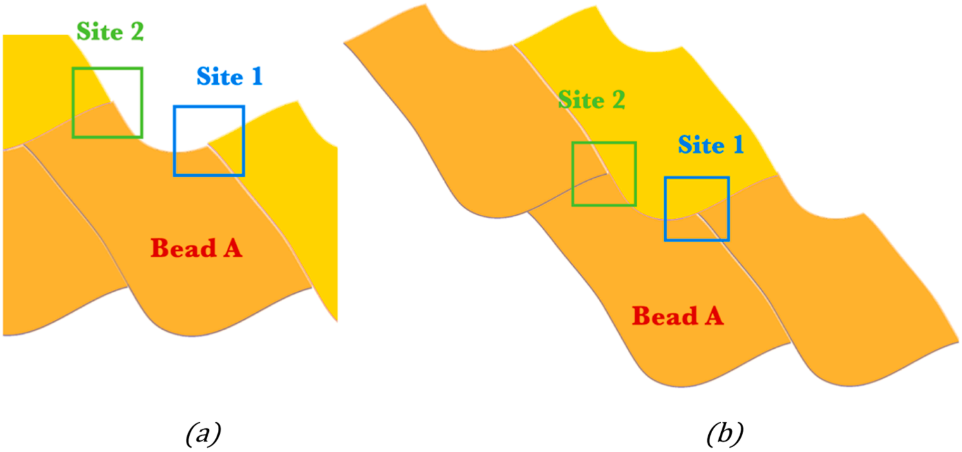

**Fig. 11.** Effects of bead deposition chronology on Site 1 and Site 2 simulations.

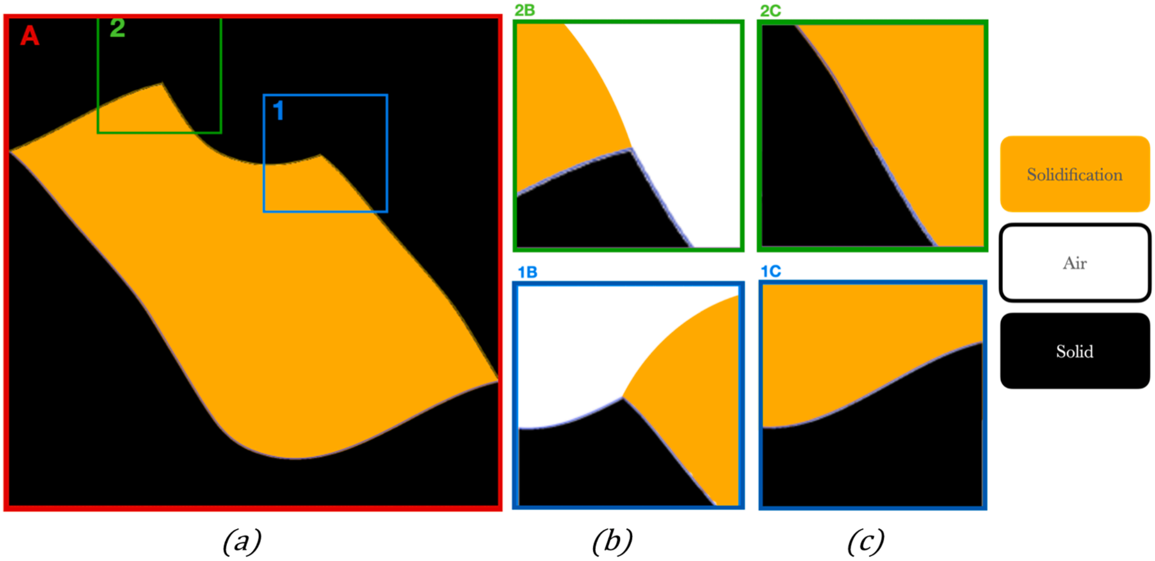

**Fig. 12.** Boundary and initial conditions applied to first and second simulation on Site 1 and Site 2.

defined.

First a simulation of bead A is performed using a coarse mesh (dx = 0.2, as in M4), and the corresponding results from method M4 for these regions of interest are retrieved (thermal field, phase field, and orientation values) (Fig. 11: site 1 and 2). These values are then reused as starting points for two new simulations concerning zone 1 and zone 2. As the dimensions of the zones are four times smaller than the initial bead A, a finer mesh can be chosen (dx = 0.05). Linear interpolation is proposed by FiPy. Although the initial coarse mesh was already satisfactory in terms of convergence, reducing the element size allows for an increased number of grains initially implanted in the simulation. Indeed, the use of phase fields is effective when the liquid-solid interface is not smaller than 5dx. Reducing the element size allows for more grains, smaller in size, to be placed at the beginning of the simulation, which should provide more information on grain selection and the effects related to seed density.

A dx value of 0.2 enables the simulation of a complete bead within a reasonable computational time, while a smaller value of 0.05 was selected for the analysis of crystal growth continuity, as it allows for the consideration of smaller "grains," which is particularly important when examining crystal growth from an existing "substrate" or an existing first bead.

The simulation applies the same conditions as those used in M4 to ensure the preservation of the solidifying molten steel's mass, where white, black, and yellow respectively represent air, solid material, and liquid. When simulating boxes 1B and 2B, it is crucial to accurately define boundary and initial conditions based on the chronological order of bead deposition. In box 1B, the right bead is deposited next in the sequence, while in box 2B, it is the bead above (Fig. 12b). Once this initial step is simulated, new conditions are then applied to complete the grain growth simulation in boxes 1C and 2C, considering the presence of the bead above for box 1C and the right bead for box 2 C (Fig. 12c). The simulation concludes upon reaching the final temperature of 450 K, at which point the results can be analyzed.

## 4. Results

### 4.1. Contour extraction and zones

Let's begin by focusing on the distribution of contour shapes in the transverse section. The contours of the beads can be categorized into three groups: those without defects, those with defects on the right side of the bead, and those with defects on the left side. Fig. 13a-c depict typical lower bead contours obtained through segmentation (method M0), represented by dashed lines, along with the corresponding mean values shown as continuous colored lines. The contours exhibit distinct shapes depending on the category they belong to, with or without defects. Specifically, in the group with defects on the right side, there is an

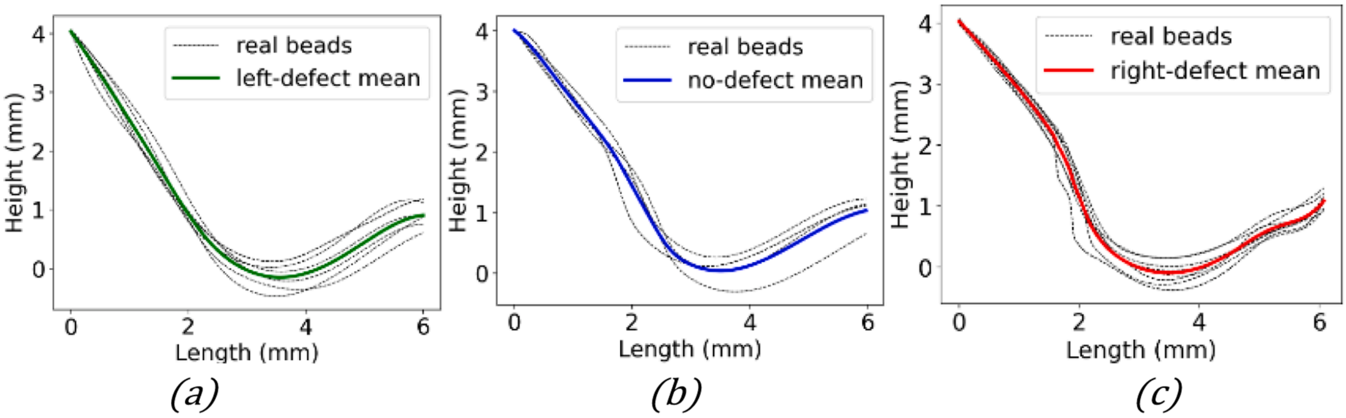

**Fig. 13.** Results of method M0. Typical bead shapes for the three types (defect to the left, without defect and defect to the right). Dashed lines represent different results obtained by segmentation. The thick colored lines represent the mean bead shape obtained as the mean value of the different cubic splines.

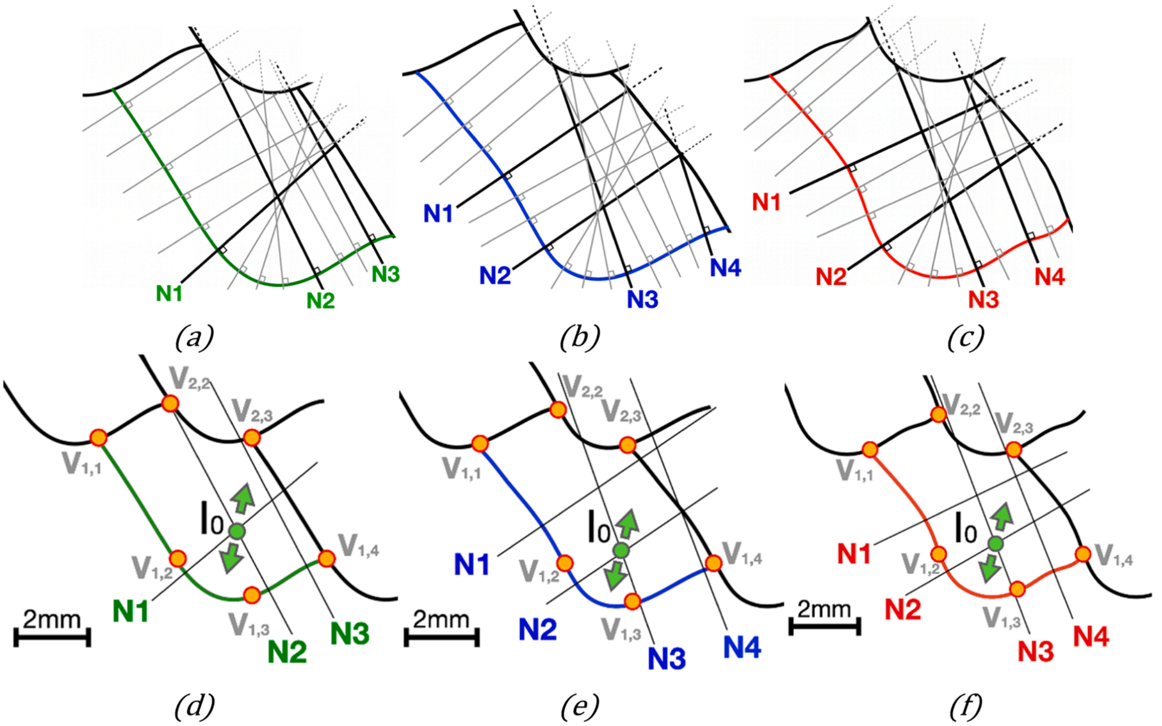

**Fig. 14.** Results of methods M1 and M2. Construction of a complete bead by starting with the lower part. The same method is applied to beads with defects to the left (a), no defect (b) and defects to the right (c). The vertices $V_{1,i(i=1,2,3,4)}$ represent the lower boundary of the current bead predicted by M0. $V_{2,2}$ and $V_{2,3}$ result from the translation of the lower bead contour. Figures (a, b, c) display the normals to the lower contours and figures (d, e, f) exhibit zones with a unique normal and zones where 2 or more normal cross.

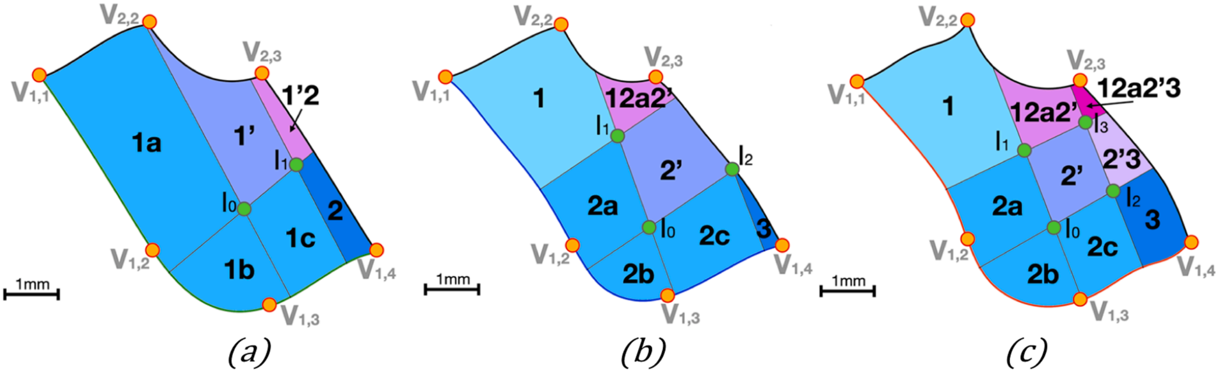

**Fig. 15.** Results of method M1. Predicted grain growth direction zones with defect on the left (a), without defect (b), with defect on the right (c).

additional curvature present to the right of the contour. Conversely, in the group with defects on the left side, there is no curvature observed on the left portion of the contour.

Fig. 14a-c display the lower contours along with their corresponding normals. The primary normals, depicted as thick black lines (N1,. N4), are drawn at points where a change in local curvature occurs. As a result, the crystal growth directions, perpendicular to the lower bead border, undergo significant changes at each of the points N1,. N4. The specific location of the primary normals strongly depends on the type of lower bead. The thin black lines within each region were utilized as input for method M3. Moving on, Fig. 14d-e showcase the three bead types reconstructed by method M1, with the vertices $V_{2,2}$ and $V_{2,3}$ determined through M1. Only the primary normals are illustrated. The subsequent figure illustrates how these lines were employed in method M2 to determine the crystal growth directions.

Fig. 15 illustrates the construction of three typical beads, with zones determined by the primary normals N1 to N4. The grain growth initiates from the lower (colored) section of each contour. In the regions adjacent to the lower contour, the crystal growth direction is uniquely determined by the normal to the contour. At this stage, the position of point I0 is not fixed. The mobility of point I0 is influenced by factors such as the cooling rate and solidification speed, which impact the grain orientation. Faster cooling results in straighter grains, while slower cooling allows more time for grain misorientation. These regions, common to all bead types, are represented in blue. However, in all other regions, competitions between different growth directions occur. This competition is indicated by a prime symbol (') or multiple digits. For example, $1'$ indicates competition between directions 1a and 1c, $2'$ indicates competition between directions 2a and 2c, and $1'2$ indicates competition between directions $1'$ and $2'$.

### 4.2. *Mapping and continuity (method M2)*

A single perfect bead maps the two-dimensional space, enabling the

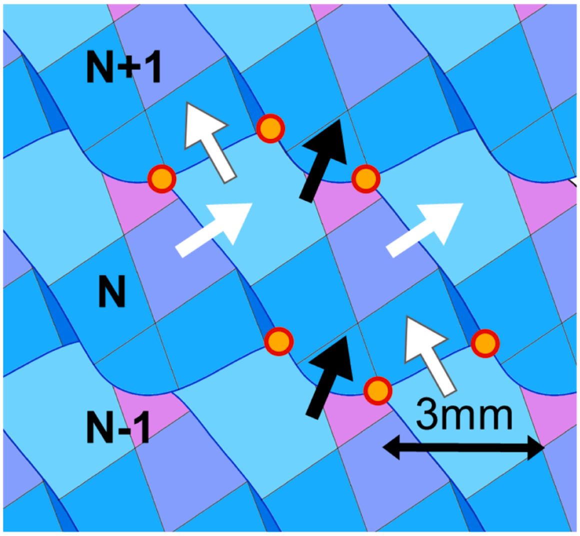

**Fig. 16.** Results of method M2. Mapping the entire plane with the flawless bead shape. Detection of possible continuity (white arrow and white arrow with black contour) or not (black arrow) crystal growth.

identification of adjacent zones when multiple beads are connected (see Fig. 16). Curved interfaces between beads do not maintain the growth directions of the crystals. These interfaces are indicated by black arrows. Now, let's focus on the zones separated by a straight interface. If nucleation occurs in the adjacent zone, it should result in a consistent crystal orientation. Nevertheless, as the remelting size increases, the possibility of misalignments between two adjacent zones also increases. Within the same layer N, the remelted zone between successive beads is small, thus making it highly probable to have identical crystal orientations. This is demonstrated by the white arrows in Fig. 16. On the other hand, significant remelting takes place between successive layers (N, N + 1), leading to a low likelihood of preserving crystal orientations, even for straight boundaries. This is indicated by white arrows with a black contour.

### 4.3. Microstructure continuity by CNN (method M3)

As a result of M1, in Fig. 11, Site 2 of bead (A) (deposited earlier) should exhibit an orientation similar to that of Site 1 of bead B. Method M3 (CNN) enables the analysis of microstructure continuity based on SEM observations. Fig. 17a,b illustrate the selected Zones of Interest (ZOI) (im1 and im2) in the SEM images. The neural network identifies continuity between the regions separated by a straight interface, while it recognizes two distinct zones when separated by a curved interface. This

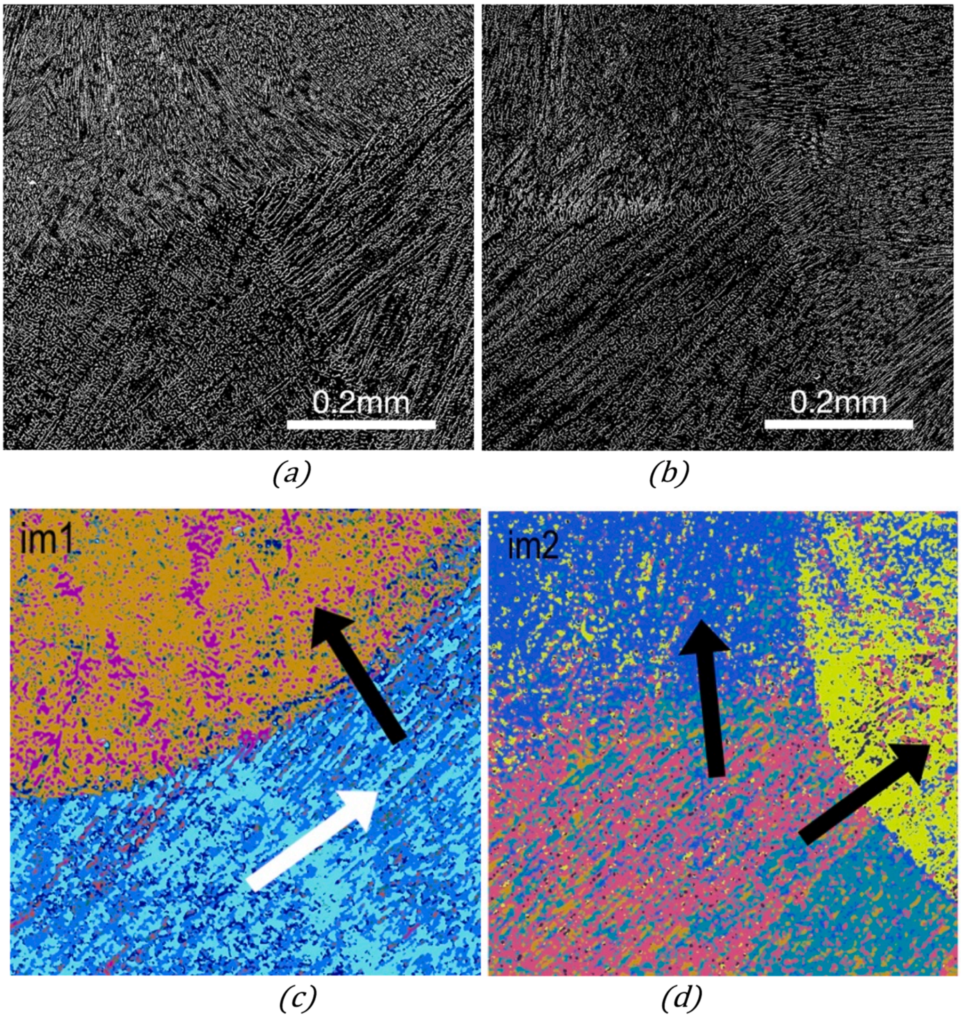

**Fig. 17.** Results of method M3. Check continuity of the microstructure. (a) and (b) SEM ZOIs used as input to the CNN algorithm: im1 (a), im2 (b), with the ZOIs result corresponding to Z0I im1 and (c) result corresponding to ZOI im2 (d). White arrows indicate continuity of the microstructure, and black ones, discontinuity, i.e., different zones.

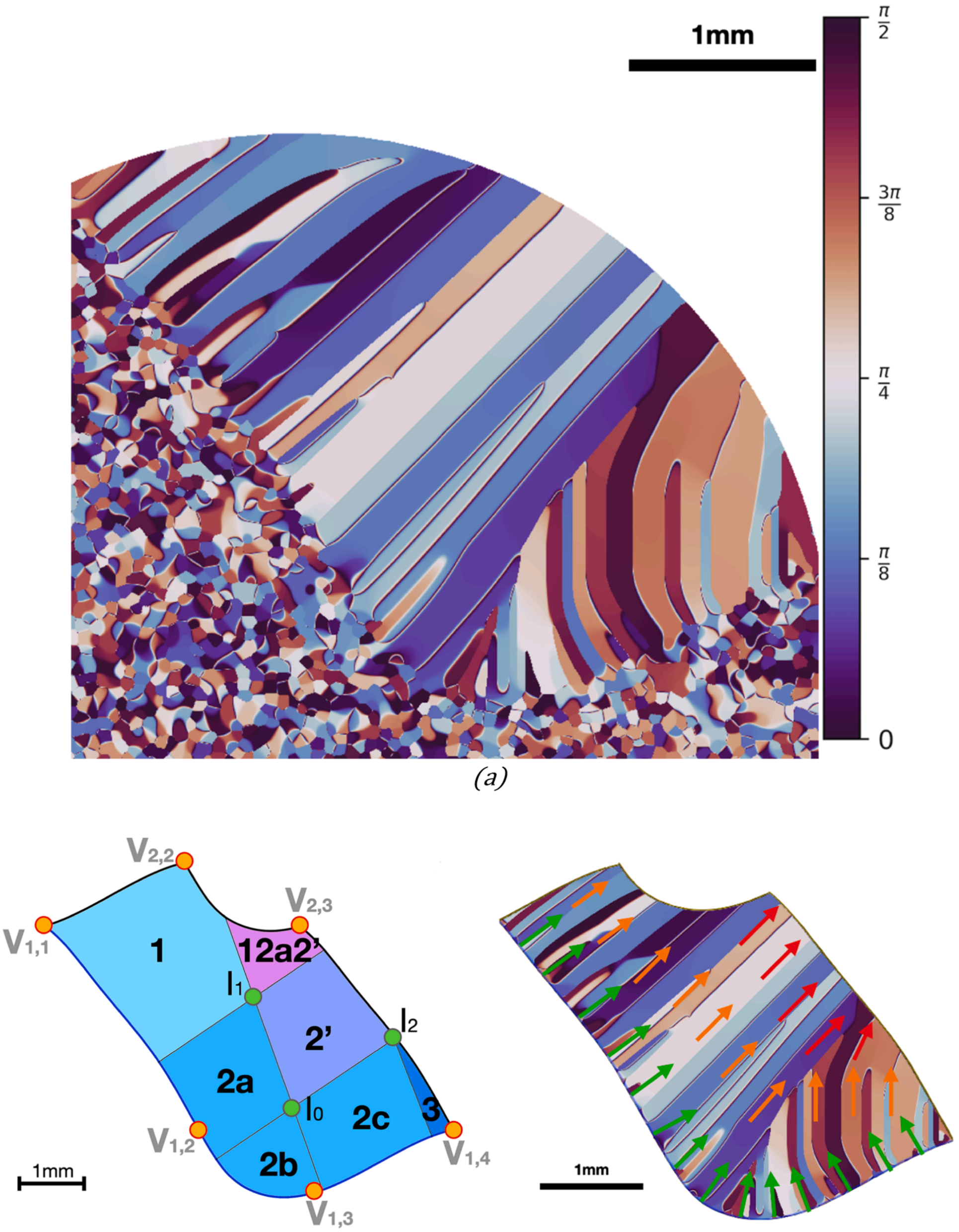

*(a)*

*(b)* *(c)*

**Fig. 18.** Crystal orientations in the real-size welding bead. (a) Phase field predictions showing the nucleation and the full droplet of 316 L, (b) crystal orientations predicted by methods M1,M2 and (c) phase field predictions.

validates the hypothesis of continuity. Additionally, we observe that the network is capable of detecting other information beyond just the growth direction. It can identify the thickness and shape of ferrite dendrites.

### *4.4. Phase field simulation of solidification (method M4)*

The phase field method serves to confirm certain predictions made by previous methods based on the geometry of weld beads. In the early stages of solidification, beyond a certain average temperature within the bead, the grain growth rate becomes large and prevents crystal deviation (Fig. 18a). The grains then grow perpendicular to the contour from which they originated (green arrows in Fig. 18c). As the temperature decreases beyond a certain threshold, solidification slows down, and the grains gradually align themselves in the direction of the resulting thermal gradient (orange and red arrows in Fig. 18c). Another phenomenon to consider is grain growth at the edge of the droplet, at the interface with the surrounding cold air. Although the thermal diffusion coefficient of air is much smaller than that of the liquid, it still plays a significant role in forming a protective crust (Fig. 18a). Additionally, it is observed that if a grain is favorably oriented relative to the neighboring growing grain, it continues to grow, while unfavorable orientation leads to its stagnation or disappearance.

We can confirm the presence of the zones predicted by M1 (Fig. 18b). Furthermore, we can now obtain more precise information about the upper zones, which are subject to grain growth competition and changes in the direction of the thermal gradient.

The predictions of method M4 are compared to EBSD characterizations in Fig. 19. For the simulation results of the M4 method (Fig. 19), the grain growth directions appear to correspond with the experiment. In the molten pool, the grains undergo radial growth and selection (Fig. 19a,b). Transition into a rectilinear growth is observed on the

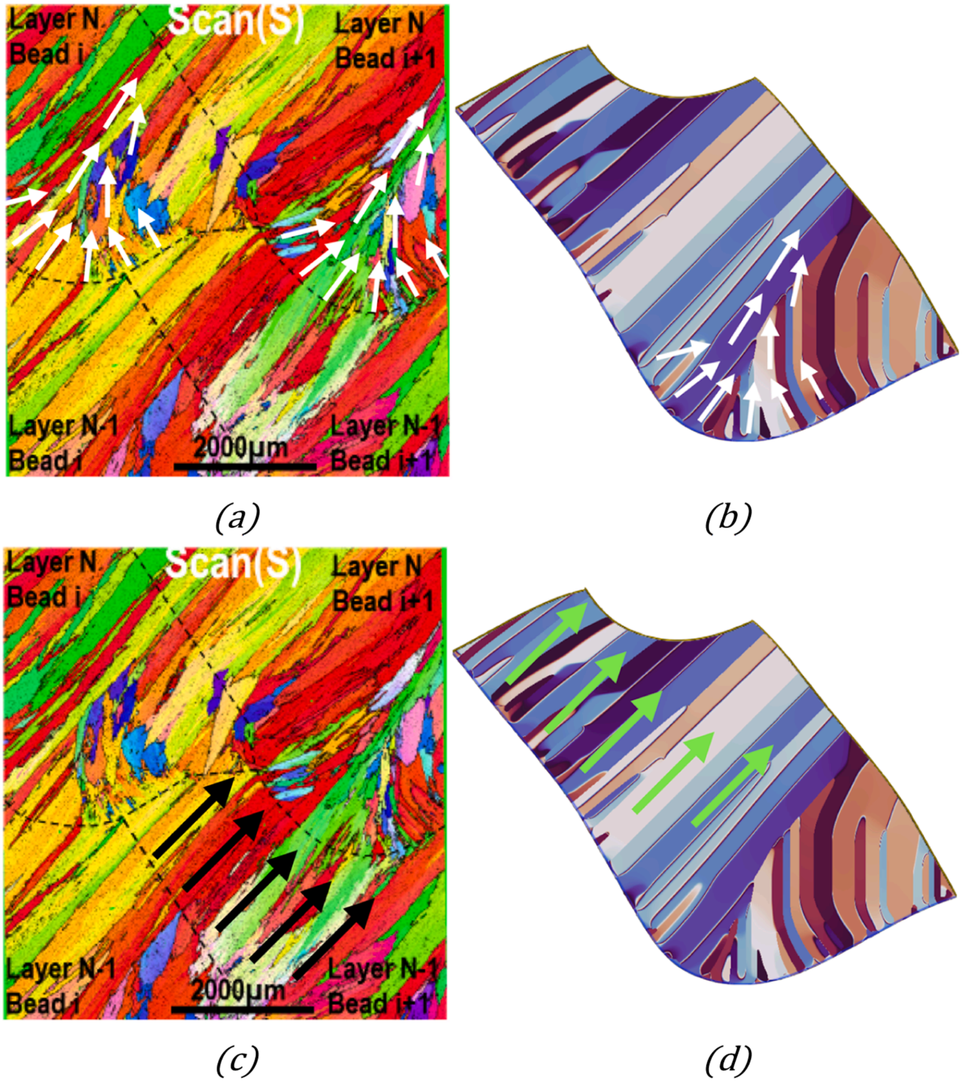

(a) (b)

(c) (d)

**Fig. 19.** Comparison between EBSD and simulation of crystal growth directions in the molten pool (a and b) and in the upper part of the beads (c and d).

upper part of the bead (Fig. 19c,d).

### 4.5. Phase field simulation of interfaces (method M5)

The objective of method M5 is to verify the hypothesis of continuity at the interfaces between weld beads. Through the creation of growth zones, mapping, and zone recognition using artificial intelligence, an assumption was made regarding the continuity of crystal growth across a flat interface between two sequentially deposited beads, and a discontinuity at curved interfaces (indicative of a remelted zone).

This hypothesis is confirmed by the PF simulations combined with the mapping shown in Fig. 19. To limit numerical simulation time, continuity was analyzed on beads extending over 2 mm. Fig. 19a shows the PF simulation of the complete bead and the location of sites 1 and 2. Crystal orientations of grains that grew from left to right in Site 1 (Fig. 19d) and Site 2 (Fig. 19b) were preserved after the deposition of the subsequent bead. This continuity is confirmed by the EBSD maps (Fig. 19c, e). However, the fusion pool, located above in Site 1 and to the right in Site 2, correspond to the starting point of new nucleation, which hinders the growth of grains from previously deposited beads (black arrows). In Fig. 19c, close to the triple junction experimentally discontinuity of crystal growth is observed very locally. The simulation box chosen was too small to exhibit this discontinuity. At a distance about 100 µm from the triple junction, epitaxial growth is observed (white arrow).

The continuity on the right side of site 2 Fig. 20 (white arrow), at the interface with the molten pool of the last deposited bead, is not visible in the image recognition of the M3 method. However, on the SEM and EBSD images, it is evident that there exists a continuity of crystal orientation on the left side of the molten pool. Effectively, at this location, the thermal gradient is perpendicular to the interface.

## 5. Discussion

### 5.1. Contour extraction and zones

Although the number of extracted weld bead contours from the image is relatively small, we can still consider the sample to be largely representative. The shape of the weld beads exhibits strong periodicity in Wire Arc CMT. Furthermore, the position of a defect has a significant impact on the contour shape and requires the distinction between the three families of weld beads. However, there can be a discussion about the geometric criterion used to create the growth zones in Method M1. The primary normals for the zones were placed at points where the lower contour undergoes a change in curvature. This appears to be a good approximation for the lower zones of the bead (those that are directly adjacent to the contour). However, for the upper zones (simulated later using phase field methods in Method M4), the geometries of

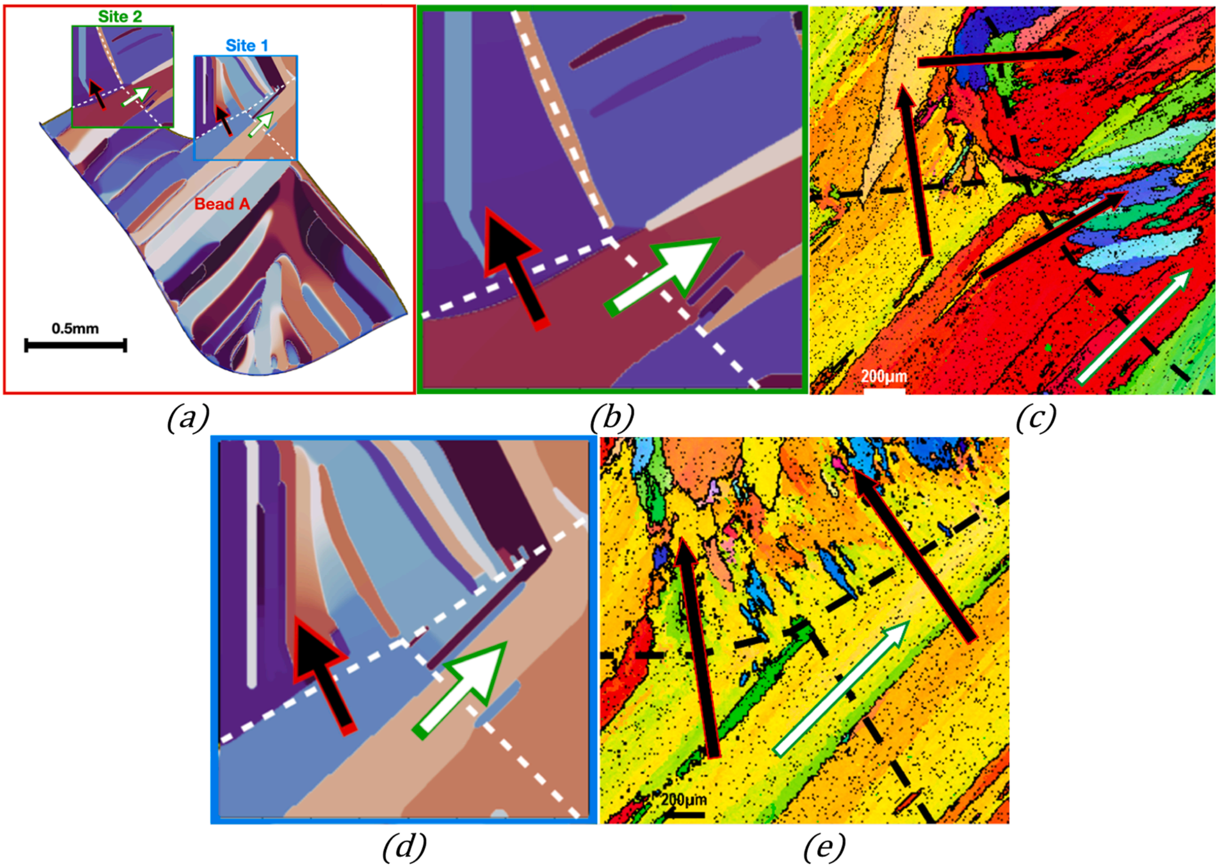

(a) (b) (c)

(d) (e)

**Fig. 20.** Results of method M5. Check continuity of the microstructure. Positions of the ZOIs used for simulations (a), phase field simulation of continuity in Site 2 (b), zoom on in EBDS map (Fig. 4) corresponding to location of Site 2 (c), phase field simulation at Site 1 (d), zoom on in EBDS map corresponding to location of Site 1 (e).

these zones may appear arbitrary. They rely on the position of the mobile point I0, which depends on the grain growth rate. In reality, the position of this point could depend on several coupled phenomena such as thermal effects or fluid mechanics. The choice to simplify the implementation of Methods M1 and M2 with this criterion was made, knowing that much more precise information could be obtained through phase field simulations.

### 5.2. *Mapping and continuity*

The use of a single SEM image is justified because the objective of this work is to present a framework based on a limited number of experimental inputs. However, it should be noted that an SEM image representing the microstructure of a weld bead is a 2D representation of a volumetric phenomenon. The crystallographic orientations determined by the EBSD observations show that the scanning direction corresponds to $< 001 >$. These results assume a steady state at a certain distance from the outer border of the block.

### 5.3. *Phase field simulations*

The present study focuses on the development of a framework for microstructure predictions, tailored specifically for the analysis of CMT (Cold Metal Transfer) processes. This framework relies on two fundamental components: Method M0 for contour extraction and Method M5 for phase field prediction. Before delving into potential further developments and enhancements, we provide an illustrative example by showcasing predictions generated using Method M5.

In Fig. 21, the initial profiles labeled (1) to (6) represent isotherms at different time points. These profiles serve as geometric input data, and Method M5 allows us to generate as many profiles as needed. Along each profile, we record the crystal orientation using pixelized information, as depicted in Fig. 21a. The pixel-by-pixel crystal orientation data along each profile is presented in Fig. 21b. This figure provides insights into the misorientation between adjacent zones. We have chosen a 15° threshold to classify a misorientation as a grain boundary. With this threshold, we can determine the number of grains for each contour. The variation in the number of grains across different contours illustrates the selection of crystal growth direction.

Finally, Fig. 21c displays a histogram of the crystal orientations observed across all the profiles. The lower profile (2) exhibits an almost random distribution, whereas profiles (5) and (6) show a distribution centered around 25°, indicating crystal growth selection. While further analyses of the phase field model predictions are certainly possible, in the following paragraph, we discuss some of the limitations and potential areas for improvement.

Let us consider the boundaries between sites 1, 2 and bead A in Fig. 19a. A small crystal misorientation between bead A and the ZOIs corresponding to sites 1 and 2 is obtained. Indeed, the thermal resolution within boxes B and C affects the grain orientation of bead A by supplying them with heat. This is what happens in a WAAM process, but over a more extended area than boxes B or C, without a break in orientation.

Another limitation is the size of the calculation boxes used to simulate grain growth at the interfaces within the ZOIs. These boxes were intentionally reduced in size to save computational time and achieve smaller element sizes (for higher accuracy). However, such a choice results in less representation of interface curvature. In a small box, a curved interface at the boundary of a fusion pool may appear flat and thus distort the interpretation of continuity. Simulations are currently

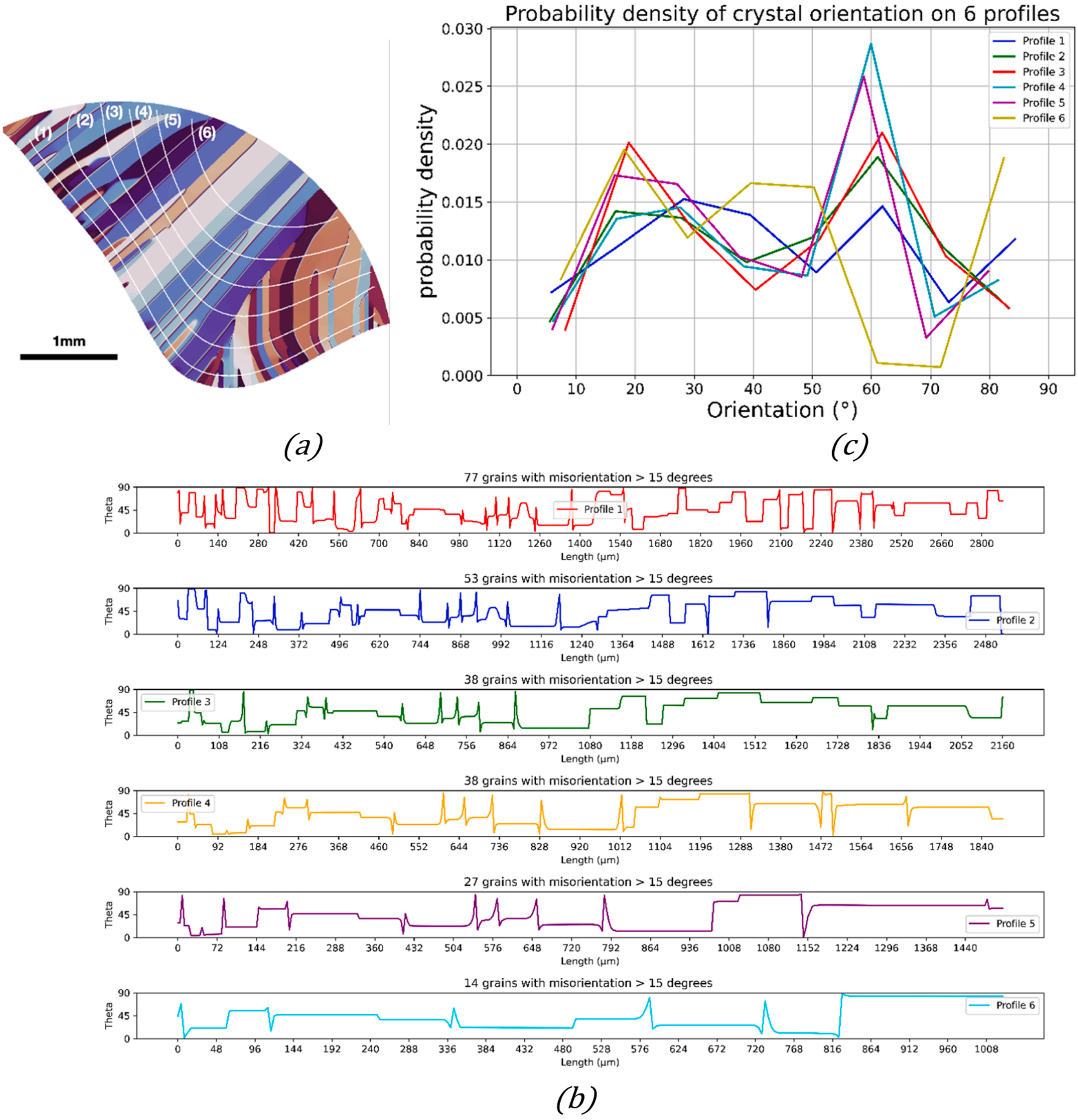

**Fig. 21.** Example analysis of phase field predictions (M_5). profiles generated for the analysis (a), crystal orientation along each profile (b), histogram of crystal orientations for profiles (2) and (5), probability density of crystal orientation on all profiles (c).

being conducted on real-sized beads with complete interfaces, which capture the full curvature between adjacent beads.

## 6. Conclusions

This paper is a practical study that employs experiments to extract information about the lower bead zones. It utilizes machine learning to estimate the distribution of orientations along bead boundaries, and then applies phase field modeling to ascertain solidification and grain orientations within the bead zones and nearby areas, especially when re-melting is considered. To illustrate the capabilities of our methodology, we used a simplified scenario of predicting grain orientations within beads made of a pure material, even though our primary focus revolves around alloys. It's conceivable that this approach can be readily extended to alloy materials. Furthermore, this research holds promise as a component of future Integrated Computational Materials Engineering (ICME) design strategies.

The present study has led to the following conclusions. Firstly, the implemented method proved to be quickly operational for predicting certain simple growth areas in a wire deposition bead. Furthermore, the use of a phase field model adapted to additive manufacturing conditions enables the prediction of the crystal microstructure of a welding bead based on its lower contour shape. Moreover, the model allows to analyze crystal orientation at bead interfaces. To the best of our knowledge this is the first study analyzing remelting with the real chronology of the wire arc deposition process.

The results obtained pave the way for interesting perspectives. A multi-phase field model assisted by artificial intelligence is under development. First, it will allow to overcome the lack of costly experimental data. On the other hand, optimized parameters for the phase field approach will be presented. These methods will accelerate the numerical methods employed in this field, thereby opening new opportunities for faster and more efficient simulations.

## CRediT authorship contribution statement

**Hussein Aboleinein:** Resources. **Helmut Klöcker:** Writing – review & editing, Writing – original draft, Validation, Supervision, Resources, Project administration, Methodology, Investigation, Funding acquisition, Formal analysis, Data curation. **Aurélien Villani:** Writing – review & editing, Software. **Antoine Herbeaux:** Writing – review & editing, Writing – original draft, Validation, Software, Methodology, Investigation, Formal analysis, Data curation, Conceptualization. **Jean-Michel Bergheau:** Writing – review & editing, Validation, Supervision. **Claire Maurice:** Validation, Methodology, Formal analysis, Data curation.

## Declaration of Competing Interest

The authors declare that they have no known competing financial interests or personal relationships that could have appeared to influence the work reported in this paper.

## Data availability

Data will be made available on request.

## Appendix

**Table 9**
Phase field model parameters dimensions. l=length, T = temperature, e=energy, t = time. Intentionally e was not replaced with the corresponding dimensions.

| | | |
|---|---|---|
| $[\mu] = l.T^{-1}.t^{-1}$ | $[D_t] = l^{-2}.t^{-1}$ | $[s] = e.l^{-2}$ |
| $[T_m] = T$ | $[\tau_\phi] = e.l^{-3}.t$ | $[a] = e^{1/2}.l^{-3/2}$ |
| $[\delta] = l$ | $[\tau_\theta] = e.l^{-3}.t$ | $[\epsilon^2] = e.l^{-1}$ |
| $[L] = e.l^{-3}$ | $[\alpha^2] = e.l^{-1}$ | $[\sigma_{l/s}] = e.l^{-2}$ |

## Appendix A. Supporting information

Supplementary data associated with this article can be found in the online version at doi:10.1016/j.addma.2024.103994.

## References

[1] W.E. Frazier, Metal additive manufacturing: a review, J. Mater. Eng. Perform. 23 (2014) 1917–1928, https://doi.org/10.1007/s11665-014-0958-z.

[2] K. Osipovich, K. Kalashnikov, A. Chumaevskii, D. Gurianov, T. Kalashnikova, A. Vorontsov, A. Zykova, V. Utyaganova, A. Panfilov, A. Nikolaeva, et al., Wire-feed electron beam additive manufacturing: a review, Metals 13 (2023) 279, https://doi.org/10.3390/met13020279.

[3] Alberto Garcia-Colomo, Dudley Wood, Filomeno Martina, Stewart W. Williams, A comparison framework to support the selection of the best additive manufacturing process for specific aerospace applications, Int. J. Rapid Manuf. Vol.9 (No.2/3) (2020) 194–211.

[4] N. Rodriguez, L. Vázquez, I. Huarte, E. Arruti, I. Tabernero, P. Alvarez, Wire and arc additive manufacturing: a comparison between CMT and Top TIG processes applied to stainless steel, Weld. World (2018).

[5] Z. Pan, D. Ding, B. Wu, D. Cuiuri, H. Li, J. Norrish, Arc Welding Processes for Additive Manufacturing: A Review 1, Springer Singapore Pte Ltd., 2018.

[6] Yan Li, Chen Su, Jianjun Zhu, Comprehensive review of wire arc additive manufacturing: hardware system, physical process, monitoring, property characterization, application and future prospects Results in Engineering 13 (2022), Results Eng. 13 (2022) 100330, https://doi.org/10.1016/j.rineng.2021.100330.

[7] Z. Zeng, B. Cong, J.P. Oliveira, W.C. Ke, N. Schell, B. Peng, Z.W. Qi, F.G. Ge, W. Zhang, S.S. Ao, Wire and arc additive manufacturing of a Ni-rich NiTi shape memory alloy: microstructure and mechanical properties, Addit. Manuf. Vol. 32 (2020) 101051.

[8] P. Long, D. Wen, J. Min, Z. Zheng, J. Li, Y. Liu, Microstructure evolution and mechanical properties of a wire-arc additive manufactured austenitic stainless steel: effect of processing parameter, Mater 14 (2021) 1681.

[9] L.L. Wang, J.X. Xue, Q. Wang, Correlation between arc mode, (2019), Microstructure, and mechanical properties during wire arc additive manufacturing of 316L stainless steel, Mater. Sci. Eng. A 751 (2019) 183–190.

[10] D. Wen, P. Long, J. Li, L. Huang, Z. Zheng, Effects of linear heat input on microstructure and corrosion behavior of an austenitic stainless steel processed by wire arc additive manufacturing, Vacuum Vol. 173 (2020).

[11] C.R. Cunningham, J. Wang, V. Dhokia, A. Shrokani, and S.T. Newman, Characterisation of Austenitic 316LSi Stainless Steel Produced by Wire Arc Additive Manufacturing with Interlayer Cooling, pp. 426–439, 2019.

[12] L. Palmeira Belotti, J.A.W. van Dommelen, M.G.D. Greers, C. Goulas, W. Ya, J.P. M. Hoefnagels, Microstructural characterisation of thick-walled wire arc additively manufactured stainless steel, J. Mater. Process. Tech. 299 (2022) 117373, https://doi.org/10.1016/j.jmatprotec.2021.117373.

[13] L. Palmeira Belotti, J.P.M. Hoefnagels, M.G.D. Geers, J.A.W. van Dommelen, A modular framework to obtain representative microstructural cells of additively manufactured parts, J. Mater. Res. Technol. 21 (2022) 1072–1094.

[14] Th Gatsos, K.A. Elsayed, Y. Zhai, D.A. Lados, Review on computational modeling of process–microstructure–property relationships in metal additive manufacturing. JOM, The Minerals, Metals & Materials Society, 2019, https://doi.org/10.1007/s11837-019-03913-x.

[15] C. Körner, M. Markl, J. Koepf, Modeling and simulation of microstructure evolution for additive manufacturing of metals: a critical review. Metallurgical and Materials Transactions 50th, 24th August, Anniversary Collection, 2020, https://doi.org/10.1007/s11661-020-05946-3.

[16] Ch-A. Gandin, Ch Charbon, M. Rappaz, Stochastic modelling of solidification grain structures, Iron Steel Inst. Jpn. Int. 35 (6) (1995) 651–657, https://doi.org/10.2355/isijinternational.

[17] C.A. Gandin, J.L. Desbiolles, M. Rappaz, et al., A three-dimensional cellular automation-finite element model for the prediction of solidification grain structures, Met. Mater. Trans. A 30 (1999) 3153–3165, https://doi.org/10.1007/s11661-999-0226-2.

[18] T. Carozzani, Ch-A. Gandin, H. Digonnet, M. Bellet, K. Zaidat, et al., Direct Simulation of a solidification benchmark experiment, Metall. Mater. Trans. A 44 (2) (2013) 873–887, https://doi.org/10.1007/s11661-012-1465-1, hal-00747567.

[19] J.A. Koepf, D. Soldner, M. Ramsperger, J. Mergheim, M. Markl, C. Körner, Numerical Microstructure Prediction by A Coupled Finite Element Cellular Automaton Model for Selective Electron Beam Melting, https://doi.org/10.1016/j.commatsci.2019.03.004.

[20] Shunyu Liu, Yung C. Shin, Integrated 2D cellular automata-phase field modeling of solidification and microstructure evolution during additive manufacturing of Ti6Al4V, Comput. Mater. Sci. Volume 183 (2020), https://doi.org/10.1016/j.commatsci.2020.109889.

[21] O. Zinovieva, A. Zinoviev, V. Ploshikhin, Three-dimensional modeling of the microstructure evolution during metal additive manufacturing, Comput. Mater. Sci. 141 (2018) 207–220, https://doi.org/10.1016/j.commatsci.2017.09.018.

[22] I. Steinbach, Phase-field models in materials science, Model. Simul. Mater. Sci. Eng. 17 (31pp) (2009) 073001.

[23] M. Plapp, Unified Derivation of Phase-field Models for Alloy Solidification from A Grand-potential Functional, Phys. Rev. E 84, 031601, 2011, Abstract. Manuscript: arXiv:1105.1670.

[24] R. Kobayashi, Modeling and numerical simulations of dendritic crystal growth, Phys. D Nonlinear Phenom. Vol 63 (1993) 410–423.

[25] A. Scotti, V. Ponomarev, W. Lucas, A scientific application-oriented classification for metal transfer modes in GMA welding, J. Mater. Process. Technol. 212 (2012) 1406–1413, https://doi.org/10.1016/j.jmatprotec.2012.01.021.

[26] A. Scotti, V. Ponomarev, W. Lucas, Interchangeable metal transfer phenomenon in GMA welding: features, mechanisms, classification, J. Mater. Process. Technol. 214 (2014) 2488–2496, https://doi.org/10.1016/j.jmatprotec.2014.05.022.

[27] J. Schindelin, I. Arganda-Carreras, E. Frise, V. Kaynig, M. Longair, T. Pietzsch, A. Cardona, Fiji: an open-source platform for biological-image analysis, Nat. Methods 9 (7) (2012) 676–682, https://doi.org/10.1038/nmeth.2019.

[28] R. Kobayashi, J.A. Warren, W.C. Carter, Vector-valued phase field model for crystallization and grain boundary formation, Phys. D. 119 (1998) 415–423.

[29] I. Hiroshige, K. Toshihiko, Solidification mechanism of austenitic stainless steels solidified with primary ferrite, Acta Materiala 124 (2017) 430–436.

[30] V.H.C. de Albuquerque, P.C. Cortez, A.R. de Alexandria, J.M.R.S. Tavares, A new solution for automatic microstructures analysis from images based on a backpropagation artificial neural network, Nondestruct. Test. Eval. 23 (2008) 273–283.

[31] V.H.C. de Albuquerque, A.R. de Alexandria, P.C. Cortez, J.M.R.S. Tavares, Evaluation of multilayer perceptron and self-organizing map neural network topologies applied on microstructure segmentation from metallographic images, NDTE Int 42 (2009) 644–651.

[32] H. Kim, J. Inoue, T. Kasuya, Unsupervised microstructure segmentation by mimicking metallurgists' approach to pattern recognition, Nat. Res. Sci. Rep. 10 (2020) 17835, https://doi.org/10.1038/s41598-020-74935-8.

[33] Achanta, R. et al., Slic Superpixels. in EPFL Technical Report No. 149300, 2010.

[34] X. Ren, J. Malik, Learning a classification model for segmentation, Proc. Ninth IEEE Int. Conf. Comput. Vis. 1 (2003) 10–17.

[35] M.Y. Liu, O. Tuzel, S. Ramalingam, R. Chellappa, Entropy rate superpixel segmentation, IEEE (2011) 2097–2104.

[36] M. Van den Bergh, X. Boix, G. Roig, B. de Capitani, L. Van Gool, Seeds: superpixels extracted via energy-driven sampling, Eur. Conf. Comput. Vis. (2012) 13–26.

[37] R. Achanta, et al., SLIC superpixels compared to state-of-the-art superpixel methods, IEEE Trans. Pattern Anal. Mach. Intell. 34 (2012) 2274–2282.

[38] J.W. Cahn, J.E. Hilliard, Free energy of a non-uniform system. 1. interfacial free energy, J. Chem. Phys. 28 (1958) 258–267.

[39] A.A. Wheeler, W.J. Boettinger, and G.B. McFadden, Phase-field Model of Solute Trapping during Solidification, Phys. Rev. E 47, 1893–Published 1 March 1993, https://doi.org/10.1103/PhysRevE.47.1893.

[40] W.J. Boettinger, J.A. Warren, C. Beckermann, A. Karma, Phase field simulation of solidifaction, Annu. Rev. Mater. Res. 32 (2002) 163–194, https://doi.org/10.1146/annurev.matsci.32.101901.155803.

[41] J.A. Warren, R. Kobayashi, A.E. Lobkovsky, W.C. Carter, Extending phase field models of solidification to polycrystalline materials, Acta Mater. 51 (2003) 6035–6058.

[42] T. Xue, Z. Gan, S. Liao, J. Cao, Physics-embedded graph network for accelerating phase-field simulation of microstructure evolution in additive manufacturing, npj Comput. Mater. 8 (1) (2022) 201.

[43] J.Y. Choi, T. Xue, S. Liao, J. Cao, Accelerating phase-field simulation of three-dimensional microstructure evolution in laser powder bed fusion with composable machine learning predictions, Addit. Manuf. (2023) 103938.

[44] Jonathan E. Guyer, Daniel Wheeler, James A. Warren, Partial FiPy: differential equations with Python. Computing in science & engineering, Inst. Electr. Electron. Eng. (2009), https://doi.org/10.1109/MCSE.2009.52.